Measuring the Thermal Properties of Organic Materials Using Time-Domain Thermotransmittance

A Thesis
presented to
the Faculty of the School of Engineering and Applied Science
University of Virginia

in partial fulfillment
of the requirements for the degree of
Master of Science in Mechanical Engineering

by

Chester J. Szwejkowski

May
2018

APPROVAL SHEET

This Thesis
is submitted in partial fulfillment of the requirements
for the degree of
Master of Science

Author Signature:

This Thesis has been read and approved by the examining committee:

Advisor: Prof. Patrick E. Hopkins

Committee Member: Prof. Mona Zebarjadi

Committee Member: Prof. David L. Green

Committee Member: Prof. Keivan Esfarjani

Committee Member:

Committee Member:

Accepted for the School of Engineering and Applied Science:

Craig H. Benson, School of Engineering and Applied Science

May 2018

Measuring the Thermal Properties of Organic Materials Using Time-Domain Thermotransmittance

by
Chester J. Szwejkowski

Presented to the Faculty of the School of Engineering and Applied Science,
University of Virginia, May 2018, in partial fulfillment of the requirements
for the degree of Master of Science in Mechanical Engineering

Abstract

Optical pump-probe measurements are routinely performed in the field of nanoscale heat transfer. The last three decades have seen much progress in the characterization of technologically relevant material systems and in furthering our understanding of the fundamental mechanisms of thermal transport. The vast majority of measurements are implemented in a reflection geometry to measure the thermoreflectance signal; however, some material systems or thermophysical properties can be easily characterized using a transmission geometry. Understanding the capabilities and limitations of thermoreflectance and thermotransmittance experiments is key to ensure good scientific practice, to push the boundaries of the experiment, and to developing new technologies. The work in this thesis represents a study on the adaptability of the time-domain thermotransmittance (TDTT) technique, particularly when applied to organic materials.

Control over the thermal conductance from excited molecules into an external environment is essential for the development of customized photothermal therapies and chemical processes. This control could be achieved through molecule tuning of the chemical moieties in fullerene derivatives. For example, the thermal transport properties in the fullerene derivatives indene-C_{60} monoadduct (ICMA), indene-C_{60} bisadduct (ICBA), [6,6]-phenyl C_{61} butyric acid methyl ester (PCBM), [6,6]-phenyl C_{61} butyric acid butyl ester (PCBB), and [6,6]-phenyl C_{61} butyric acid octyl ester (PCBO) could be tuned by choosing a functional group such that its intrinsic vibrational density of states bridge that of the parent molecule and a liquid. However, this effect has never been experimentally realized for molecular interfaces in liquid suspensions. Using the pump−probe technique time domain thermotransmittance, we measure the vibrational relaxation times of photoexcited fullerene derivatives in solutions and calculate an effective thermal boundary conductance from the opto-thermally excited molecule into the liquid. We relate the thermal boundary conductance to the vibrational modes of the functional groups using density of states calculations from molecular dynamics. Our findings indicate that the

attachment of an ester group to a C_{60} molecule, such as in PCBM, PCBB, and PCBO, provides low-frequency modes which facilitate thermal coupling with the liquid. This offers a channel for heat flow in addition to direct coupling between the buckyball and the liquid. In contrast, the attachment of indene rings to C_{60} does not supply the same low-frequency modes and, thus, does not generate the same enhancement in thermal boundary conductance. Understanding how chemical functionalization of C_{60} affects the vibrational thermal transport in molecule/liquid systems allows the thermal boundary conductance to be manipulated and adapted for medical and chemical applications.

We report the development of a novel use of the TDTT technique to characterize the nanoscale morphology of structural proteins. We also show theoretically that the thermotransmittance measurement is correlated to the protein crystallinity via the thermo-optic coefficient. As shown here, time-resolved changes in the refractive index of semi-crystalline proteins vary as a function of temperature, and the strength of this effect correlates with crystallinity. Ultimately, this allows us to quantify rapidly the crystallinity of a protein sample using TDTT by decoupling volumetric thermal expansion from its structural response at room temperature. This approach can potentially be used for screening an ultra-large number of proteins *in vivo*. The size of the library for these proteins is simply limited by the fluidic and electronic components of the sorting since the TDTT technique operates in the order of minutes to seconds. If this screening technique is achieved, we could answer many fundamental questions in protein research, such as the underlying sequence–structure relationship for structural proteins. Successful development of this technique for proteins will have a significant impact on multiple applications in various fields (e.g., materials science, synthetic biology, metabolic engineering, agriculture, prion based diseases) and open new avenues of protein research.

Acknowledgements

I have been lucky to have such great friends, family, and colleagues during my graduate education; this work would not have been possible without their amazing support.

First, I would like to thank my advisor, Prof. Patrick Hopkins, who is truly an inspiring individual. Not only are you a rock star scientist, but you are also a noble person and a true friend. You have always been understanding, patient, and willing to do whatever you can to help me get the most out of grad school. I appreciate your continuing support.

I am also thankful for the guidance of my committee members Prof. Mona Zebarjadi, Prof. David Green, and Prof. Keivan Esfarjani. Thank you for your time and for asking me the tough questions. This work is better because of it.

I am indebted to my collaborators who contributed to the work in this thesis. A big thanks goes to those at Penn. State University working with Prof. Melik Demirel for supplying me with wonderfully interesting materials to study. I know that it takes a lot of hard work from many different people to fabricate these synthetic protein structures and I am grateful that I was the one to measure them. I am also thankful to Prof. Bryan Kaehr for your expertise in fullerenes and for always offering your help in understanding them and to characterize them. And, thank you Prof. Ronald Warzoha, with whom I started working with fullerenes while we were both learning to use pump-probe thermometry. I sincerely enjoyed our time together.

I am grateful for everyone that has been a part of the ExSiTE Lab. It has been and pleasure to work with everyone and an honor to be a part of science! I would like to thank the TDTR wizard, Dr. Ramez Cheaito, for teaching me how to perform the pump-probe technique properly. Your thoroughness and patience is appreciated. I would also like to thank Prof. Brian Donovan, Dr. Brian Foley, and Dr. Ash Giri for their contribution to my understanding of TDTR. Dr. Ash Giri and Jeff Braun, you two have been supportive lab mates as well as great room mates and I value the friendship that we share. I would not have made it this far without you. BDN!

I am lucky to have had the support of many friends from many different circles. I would like to thank my groomies, Jack, Jung, Steven, Peter, Lawrence, and Danny. I can always count on you when it matters. I love you guys. Thank you to the members of the First Harmonics and to Ben and Lise for your instant friendship. Singing with you all has always been a source of enjoyment to distract me from the stress of grad school. Thanks to my friends in GESC and my fellow Ravens. Cacaw! It has been an honor serving with you and I have met more interesting people here at UVa than I could have imagined.

I am indebted to my family, ALL of my family, for always providing your love and support. I consider myself fortunate to have so many who love me unconditionally. Although we may not have spent as much time together as we want these last few years, I cherish the moments we’re together all the same.

Most of all, I thank my wife Meaghan. You have been selfless, encouraging, and loving. You have my undying love and gratitude for being by my side these last few years. There is nothing better than coming home to you and (as much as I avoid admitting it) Lucy and Pico. Let’s start our next adventure!

Table of Contents

List of Figures

List of Tables

Chapter 1

Introduction

1.1 Background

As science advances, so too does the methodology. The field of nanotechnology bears witness to this, in part due to the difficulty involved in characterizing the physical properties of nanoscale systems. As the characteristic length of a system decreases, the surface area-to-volume ratio increases and material interfaces become more influential; additionally, the characteristic time of relevant dynamic processes decreases. Eventually, the physical state or material properties in the context of bulk materials cannot be accurately determined and a consideration of fundamental energy carriers (e.g. photons, electrons, and phonons) is required. The scientific community has learned that such systems can be quite deferent from their bulk counterparts, leading to the development of new scientific theories, new technological applications, and motivating the improvement of experimental techniques.

In crystalline nonmetal materials, heat is carried by phonons (i.e. quantized lattice vibrations).[1-4] Thermal resistance is caused by these phonons scattering from boundaries, disorder, and other phonons.[1-4] The average distance between scattering events is called the "mean free path" (MFP).[1-4] In nanoscale material systems where the characteristic length is smaller than the mean free path, boundary scattering is the dominant thermal resistor.[3-5] This thermal boundary resistance R_K [W^{-1} m^2 K], or inversely the thermal boundary conductance h_K [W m^{-2} K^{-1}], causes a temperature drop ΔT at the interface between two materials given heat flux q:[5]

$$q = h_K \Delta T \tag{1.1}$$

This temperature discontinuity was first observed between copper and liquid helium in 1941 by Kapitza.[6] The thermal boundary conductance (sometimes called "Kapitza conductance"), depends on the materials that form the interface, the quality of the interface, and the composition near the interface, among other things.[5]

In this thesis, I focus on the characterization of the nanoscale thermal transport properties of organic materials using an optical pump-probe technique. Pump-probe measurements use two pulsed laser beams (the "pump" and the "probe") to investigate ultrafast phenomena. Pump pulses excite the sample, causing a change in its properties, while probe pulses are used to probe the sample after an adjustable delay time. This technique relies on the principle that the excitation of the sample from the pump will cause a measureable change in the reflection or transmission of the probe. Furthermore, the measured change in reflectance or transmittance must be relatable to the change in a useful physical quantity (e.g. temperature). A dataset from a pump-probe experiment typically consists of measurements at different pump-probe delays times, allowing one to observe the time evolution of the excitation and relaxation after a pump pulse.

The phenomenon of interest for this work is the diffusion of heat through a sample after the absorption of a pump pulse. In the limit of small changes in temperature ΔT, the change in transmittance ΔTr varies linearly according to:

$$\Delta Tr = \frac{\partial Tr}{\partial T} \Delta T = \xi \Delta T \tag{1.2}$$

where ξ is the "thermotransmittance coefficient". Using a time-dependent thermal model for ΔT, it is possible to determine the thermal properties of materials and interfaces (e.g. thermal conductivity, thermal boundary conductance, and heat capacity). The change in transmittance is related to the change in refractive index through the Fresnel equations.[7] Applying an infinitesimal change in temperature yields:

$$\frac{dTr}{dT} = \frac{4(1-n)}{(n+1)^3}\frac{dn}{dT} \tag{1.3}$$

where n is the index of refraction and dn/dT is defined as the thermo-optic coefficient, or the change in the index of refraction due to a change in temperature. Thus, the thermo-optic coefficient can be determined by making pump-probe measurements at different temperatures.

1.2 Thermal Transport

In non-metallic materials, heat is primarily carried by the vibrations of atoms.[1-4] A collection of vibrating atoms gives rise to elastic waves that can propagate through the material.[1-4] Similarly to how light has a spectrum of wavelengths, frequencies and energies, these modes of vibration make up a spectrum of wavelengths, frequencies and energies.[1-4] In a periodic crystal, we refer to these modes of vibration as phonons,[1-4] while in an amorphous material we call them extendons.[8] As an umbrella term, I will simply refer to "vibrational modes", which I consider to encompass crystalline and amorphous materials as well as molecules and macromolecules. While in the classical description these vibrational modes are described as waves, it is often mathematically convenient to adopt the quantum mechanical treatment of vibrational modes as particles; thus, vibrational modes are quasi-particles.[1-4]

Each vibrational mode has an angular frequency ω, wavevector k, and energy $\hbar\omega$, where $\hbar$ is the reduce Planck's constant.[1-4] The spectrum and number of vibrational modes that can exist in a material is often represented by the "density of states" (DOS).[1-4] This DOS is commonly shown as a function of frequency. A large DOS at a given frequency (or state) means that many vibrational modes can occupy that frequency. A DOS of zero means no vibrational modes exist at that frequency. The occupation of each state is dictated by a statistical distribution function which is temperature dependent.[1-4] Vibrational modes obey Bose-Einstein statistics:[1-4]

$$f_{BE}(\omega) = \frac{1}{\exp\left(\frac{\hbar\omega}{k_B T}\right) - 1} \tag{1.4}$$

where k_B is the Boltzmann constant. If we sum up all of the energy from each vibrational mode according to the Bose-Einstein distributed occupation of the DOS, we can calculate the thermal energy U_{th} in a material as follows:[1-4]

$$U_{th} = \int_{\omega} \hbar\omega\mathcal{D}(\omega) f_{BE}(\omega, T) d\omega \tag{1.5}$$

where $\mathcal{D}$ is the DOS and T is the temperature. Note, the summation over different branches and polarizations is implied in this introduction. Heat capacity is the ability of a material to store internal energy in response to a change in temperature. Mathematically, this is represented as the following:[1-4]

$$C = \frac{\partial U_{th}}{\partial T} = \int_{\omega} \hbar\omega\mathcal{D}(\omega) \frac{\partial f_{BE}(\omega, T)}{\partial T}\, d\omega \tag{1.6}$$

where the derivative only applies to the Bose-Einstein distribution since it is common to assume there are no other temperature-dependent terms at low and moderate temperatures.

Temperature gradients exist within a material because the thermal conductivity, or the efficiency at which a quantity of heat can traverse a material, is finite.[1-4] In other words, vibrational modes cannot carry heat indefinitely. In the particle picture, vibrational modes undergo "scattering events" which give rise to thermal resistance (finite thermal conductivity).[1-4] Vibrational modes are scattered by primarily boundaries, disorder, and other vibrational modes.[1-4] The average distance a vibrational modes travels between scattering events, λ_{MFP}, is called the "mean free path".[1-4] A vibrational mode with mean free path λ_{MFP} traveling at velocity v will have a scattering time of $\tau = \lambda_{MFP}/v$.[1-4] We can now define the thermal conductivity according to the kinetic theory of gasses:[1-4]

$$\kappa = \frac{1}{3} C v \lambda_{MFP} = \frac{1}{3} \int_{\omega} \hbar\omega \mathcal{D}(\omega) \frac{\partial f_{BE}(\omega, T)}{\partial T} v(\omega) \lambda_{MFP}(\omega, T, L)\, d\omega \tag{1.7}$$

where L is the critical dimension of the material in reference to boundary scattering. Note, we could easily substitute in scattering time instead of mean free path.

A similar concept is used to describe the efficiency at which a quantity of heat can traverse an interface between two materials; this is called the "thermal boundary conductance" (sometimes referred to as "Kapitza conductance").[5-6] This is thermal boundary conductance is the proportionality constant between the heat flux across an interface, q, and the temperature drop near said interface ΔT.[5-6] Thus, we have the equation:[5-6]

$$q = h_K \Delta T \tag{1.8}$$

where h_K represents the thermal boundary conductance. In nanoscale materials systems where dimensions are on the order of or smaller than the mean free paths of the vibrational modes (~10 nm to 100 nm), the thermal boundary conductance will dictate the thermal transport characteristics.

1.3 Optical Pump-Probe Thermometry Techniques

The advancement of laser technology pushes the limit of what conditions are achievable in the laboratory and allows scientists to observe new and interesting phenomena. In the field of nanoscale heat transfer, pulsed lasers have been used for the last three decades to measure the thermal properties of materials using a pump-probe scheme,[9-13] with major developments taking place with the introduction of the famously-tunable titanium-sapphire laser. The pump-probe technique I use throughout this work is a two-step measurement (excitation by the "pump" and detection by the "probe") with a pulsed laser beam for both the pump and probe. The path length difference between the pump and probe beams, which is proportional to the temporal separation between pump and probe pulses, can be adjusted throughout the data collection process using a mechanical delay stage which translates a mirror through space. The temporal different between the arrival of pump and probe pulses is called the "delay time". A pump pulse incident on the sample is absorbed, resulting in an excited state. In the excited state, the optical properties of the sample evolve, eventually relaxing back to the ground state. The reflection or transmission of a probe pulse incident on the sample is detected at different delay times during this excitation and relaxation process, providing a dataset in the time domain. In the limit of negligible absorption of the probe beam and small temperature excursions from pump beam, the relationship between the reflectance and temperature rise is as follows:

$$\Delta R = \frac{\partial R}{\partial T}\Delta T = \beta\Delta T \tag{1.9}$$

where, β is the thermoreflectance coefficient. Alternatively, making the same assumptions about the influence of the pump and probe, we can state this in terms of transmittance:

$$\Delta Tr = \frac{\partial Tr}{\partial T}\Delta T = \xi\Delta T \tag{1.10}$$

where, ξ could be called the "thermotransmittance" coefficient.

Credit for the first application of this technique for thermal measurements is usually given to Paddock and Eesley who used the thermoreflectance to determine the thermal diffusivity of metal films and metallic alloys in 1986.[9-10] While they called their experiment "transient thermoreflectance" (TTR), the name "time-domain thermoreflectance" (TDTR) is used by the nanoscale heat transfer community to distinguish the use of the out-of-phase signal from high repetition rate laser systems.[14] It is worth mentioning that using the thermoreflectance to measure the thermal properties of a sample typically requires a thin metal film (e.g. ~100 nm aluminum) to act as a transducer, converting optical energy into thermal energy.[15-17] Since Paddock and Eesley's work, numerous groups have used improvements and variations of TDTR to explore thermal transport,[18-21] electron-phonon coupling,[22] magnon dynamics,[23] and acoustic wave propagation.[24-25] One such piece of work, which has been particularly influential to my research, was that of Huxtable *et al.* who used thermotransmittance measurements to observe the relaxation of vibrational energy in fullerene suspensions.[26] By simply measuring the thermotransmittance rather than the thermoreflectance, they were able to extend their measurement capabilities to include nanofluids and discard the requirement of a metal transducer layer. Although this technique has been called “transient absorption” in the past,[26-29] I refer to this as “time-domain thermotransmittance” to be consistent with the name of TDTR and to reflect the conceptual similarity of the two techniques.

1.4 Applications

Photothermal Therapy

Photothermal therapy (PTT) is a medical technique in which particular cells are targeted and ablated using a photothermal agent (PTA) to convert light into heat.[30-34] The challenge is in choosing a PTA which will only congregate at the desired target area, requires low energy light (usually near infrared) to avoid collateral damage, and effectively transduces optical energy into thermal energy.[30-34] Characterizing these properties of potential PTAs has been the focus of much research in the last decade,[30-34] progressing PTT to the clinical trial stage for cancer treatment.[30-34] While the first advancements in PTT used gold nanorods as PTAs,[30-34] organic molecules have recently received attention in nanoscale thermal transport studies.[26, 35-36] The relevant property for these systems is the thermal boundary conductance between the PTA and its surroundings,[26-29, 35-36] which indicates the ability to conduct heat between the PTA and the surrounding environment. The capability to engineer the thermal properties of PTAs would extend the conditions for which PTT can be applied.

Thermo-optic Switch

A material's index of refraction dictates the transmittance and reflectance of light.[7] The ability to dynamically change the index of refraction of a material is widely exploited in optical modulators and switches for laser systems and fiber optics.[37-41] The thermo-optic effect is the change in the refractive property of a material induced by a change in temperature.[37-42] A material with a large enough thermo-optic coefficient can be used to fabricate a switching device that requires minimal input power.[37-41] Thermo-optic variations of such switches are considered high performing due to their small size, scalability, and waveguide (fiber) compatibility. While polymers and silica are historically popular for thermo-optic switches,[37-41] semiconductors and more exotic materials (proteins) have recently become attractive.[37-42] The optical properties of such materials are highly tunable via a variety of fabrication techniques and processing conditions, allowing one to control the thermo-optic response of the switch.[37-41]

Abnormal Cell Detection

The thermo-optic coefficient of materials has a nonlinear dependence on the crystalline fraction (the portion of the material that has a well-defined crystal structure versus a random amorphous structure).[42] This relationship holds true for proteins.[42] Different tissues in the human body have different specializations, which is reflected in the types of proteins that the cells from that tissue produce.[43] By characterizing the thermo-optic response of different protein aggregates, a catalog can be created to identify cells of different types or detect cells with abnormalities. The thermo-optic coefficient can be measured in a matter of minutes, possibly seconds, with a well-calibrated system.[42] This type of characterization could be utilized as a type of screening for cell abnormalities prevalent in diseased tissue with the potential to produce results faster than traditional methods.

1.5 Statement of Objectives and Scope

The major objectives of this work are to (1) determine the advantages and disadvantages of the TDTT technique versus the TDTR technique, (2) develop an understanding of the fundamental mechanisms of thermal transport in fullerene nanofluids, and (3) relate the measureable quantities in TDTT experiments on protein films and cell solutions to their properties and structure. While the systems studied in this thesis are limited (fullerene nanofluids, protein films, and cell solutions), the potential for the TDTT technique and the impact of these results are broad. The remainder of this thesis is organized as follows:

- *Chapter 2* All the thermal measurements in this work were conducted using time-domain thermotransmittance (TDTT), an optical pump-probe thermometry technique well-suited for thermal measurements of nanoscale material systems. A derivation of the thermal model used for nanofluids is given. Sources of error are discussed.
- *Chapter 3* Diffusive thermal transport in fullerene solutions is demonstrated. The thermal boundary conductance between fullerene molecules and the surrounding liquid is discussed in terms of the bridging between vibrational modes in the molecule and the liquid.

- *Chapter 4* TDTT measurements of protein films are related to the thermo-optic coefficient and the crystalline index. Measurements are compared to solutions of *E. coli* cells which have been programmed to overexpress corresponding protein varieties. The application for cancer screening is discussed.
- *Chapter 5* The major points of this thesis are summarized and the impact of these findings are discussed. Future projects are proposed based on these findings.

Chapter 2

Measurement Method: Time-Domain Thermotransmittance

2.1 Background

In Chapter 1, I briefly introduced pump-probe thermometry techniques. Time-domain thermoreflectance (TDTR) has become a standard in the nanoscale heat transfer community for measuring the thermal transport in thin films and across interfaces.[11-13] Although Paddock and Eesley's original measurements in 1986 used two dye lasers to form the pump and probe beams,[9-10] a single Ti:Sapphire laser is now used in TDTR (first major improvements by Cahill and coworkers in 2002)[13] for its spectral tunability, short pulse widths (~150 fs), stability, low amplitude noise, and high power output. Cahill *et al.* made several improvements including a geometry which allowed for a single objective lens to focus the pump and probe beams, a charge-coupled device (CCD) camera to visualize the beam spots on the sample, and an inductive resonator in series with the photodetector to increase the signal-to-noise ratio (SNR).[12-13, 15, 44-47] This thermoreflectance setup was modified by Wilson *et al.* in 2002 to accommodate transmission measurements and used it to make the first time domain thermotransmittance (TDTT) measurements of nanofluids.[29] In 2008, Schmidt *et al.* developed a system with two distinct features: a frequencydoubling bismuth triborate (BiBO) crystal to convert the 800 nm wavelength pump beam to 400 nm and reduce optical noise, and beam expander lens pair to increase the size of the probe beam along the delay stage and minimize divergence of the probe.[17, 48-49] We have built a pump-probe system in the ExSiTE Lab at the University of Virginia that incorporates features from the systems listed above, creating a state-of-the-art setup which I have used for all of the measurements in this thesis.

2.2 Experimental Setup

A schematic with the major components of our TDTT system is shown in Figure 2.1. The system begins with a seeded Ti:Sapphire laser which emits a train of ~100 fs pulses at a repetition rate of 80 MHz (12.5 ns between pulses) with a spectral output centered at 800 nm (~10 nm FWHM) and an average power of ~2 W. The beam is passed through an optical isolator to prevent back reflections from destabilizing the laser, after which several mirrors are used to raise the beam to a more convenient working height (not shown). One of the output ports of the isolator is collected with a spectrometer to monitor the spectral output of the laser. The beam is then divided into the pump and probe beams using a $\lambda/2$ waveplate and a polarizing beam splitting (PBS) to control what fraction of light is designated for each path.

The probe beam, which will ultimately be detected to make the measurement, is always aligned first as it is more convenient to overlay the pump beam once the detection optics are aligned. Once concern for long optical path lengths is divergence of the beam, which results in an inconsistent TDTT measurement.[48] Since the degree of divergence is

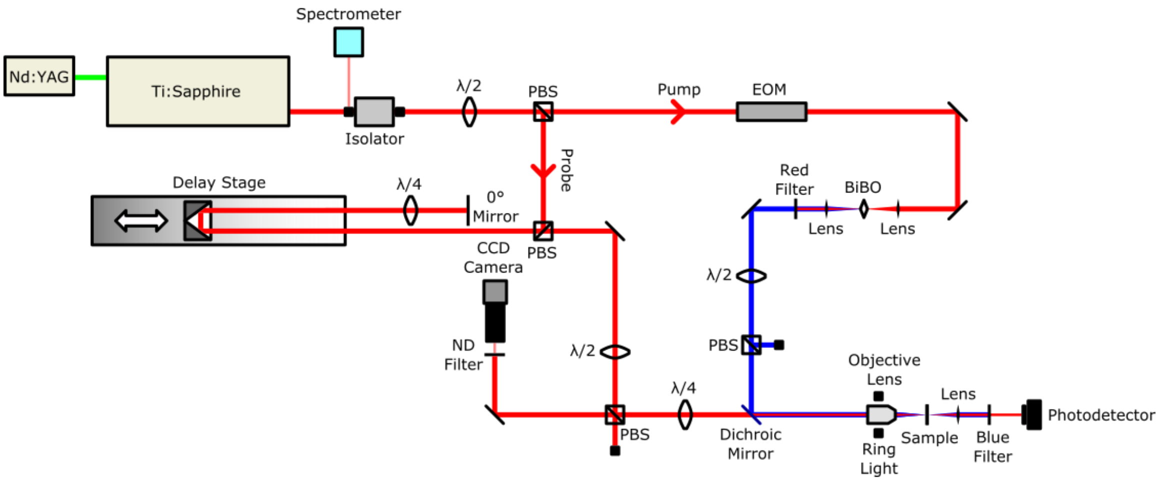

Figure 2.1. A schematic with the main components of the TDTT system. The pulse train from the Ti:Sapphire laser is split into pump and probe beams. The pump beam is amplitude modulated by the EOM, resulting in a modulated heating event on the sample. Probe pulses are varied in delay time using the delay stage, allowing time domain information to be collected. The two-color scheme (blue pump, red probe) alleviates optical noise from the pump entering the photodetector.

inversely proportional to the size of the beam, a large beam diameter is desired.[48] A pair of lenses is used expand the diameter of the probe beam before it enters the delay state. This is later reversed with another lens pair after the delay stage (expanding/compressing lenses not shown). A PBS directs the probe to the delay stage which consists of a retroreflector on a motorized stage. A 0° mirror and a $\lambda/4$ waveplate return the probe to the delay stage such that the previous PBS will now transmit, rather than reflect, the incoming probe beam. This double-pass delay stage arrangement allows for delay times up to ~7 ns (~2 m path length difference) with resolution limited by the pulse width (~100 fs). Another $\lambda/2$ waveplate and PBS are used both as a final knob to control the probe power and to direct the probe towards the sample. An objective lens equipped with a ring light focuses the probe onto the sample, after which another lens focusses the transmitted probe beam onto a photodetector.

The pump beam is first sent through an electro-optic modulator (EOM) which applies a square-wave modulation to the amplitude of the pump beam intensity at frequencies up to ~20 MHz. This in turn causes a modulated heating event on the sample, which results in a modulation of the transmitted probe beam. After the EOM, the pump is focused onto the BiBO using a lens, converting a portion of the pump beam into 400 nm light. The beam is then collimated using another lens and the remaining 800 nm light is removed with a red filter. Similarly to the probe, a $\lambda/2$ waveplate and PBS are used to control the pump power. Then, a dichroic mirror, which transmits the 800 nm light of the probe but reflects the 400 nm light of the pump, steers the pump to the objective lens in such a way that it overlaps with the probe spot on the sample. Any pump light that transmits through the sample is filtered out using a blue filter before the photodetector.

Before measurements, the sample is brought to the focal plane of the objective lens using a multi-axis stage. The spots size of the pump and probe at this position are predetermined using a commercial beam profiler (Thorlabs BP209-VIS/M). Typical $1/e^2$ radii for the pump and probe are ~20 and 10 μm, respectively; although these can be adjusted using the compressing lens pair for the probe and the lens after the BiBO for the pump. For small spot sizes (< 5 μm), a knife-edge measurement may be more accurate; however, using large spot sizes like those mentioned above reduces the effects varying spot size or shape.[7, 14-15] Backreflected light from the sample is utilized for visualizing the pump and probe spots on the sample with a CCD camera. Rail mounting is used to keep the focusing lens, blue filter, and photodetector aligned with the probe after the sample. The pump and probe can be overlapped by steering the pump with the dichroic mirror in conjunction with the beam profiler, CCD camera, or by maximizing the magnitude of the detected thermotransmittance signal.

Detecting a thermotransmittance signal from a photodetector requires the use of a lock-in amplifier.[15-17] This is because the change in transmittance with temperature is extremely small ($< 10^{-4}$), and the signal from this change is lost in the large “direct current” (DC) background of the transmitted probe beam.[7, 14-15] Using the same signal that drives the EOM to modulate the pump as a reference signal, a lock-in amplifier allows us to detect the phase and amplitude of signals at this same frequency.[7, 14-15] To improve the SNR even further, an inductive resonator is used in series with the photodetector to filter out additional unwanted components of the signal, leaving only the fundamental sinusoid; this inductive filter also increases the Q-factor of the resonant circuit use for detection by a factor of ~10.[25] An example of this idealized heat input and measured response is shown in Figure 2.2.

The lock-in amplifier is a phase sensitive detection system which requires a reference signal (the signal driving the EOM) to detect measured responses (probe beam input to the photodetector) at the same frequency of the reference.[50] The lock-in provides the magnitude and phase shift of the measured signal compared to the reference signal or, alternatively, the magnitude and phase can be deconstructed from the phasor information into in-phase and out-of-phase signals, V_{in} and V_{out}, respectively.[50] Because the electronics used in the setup add an additional phase offset to the measurement, using V_{in} and V_{out} requires an additional step in the post processing of the gathered data to correct the phase information.[7, 14-15] Typically, V_{in} is thought of as the “impulse response” of the signal while V_{out} is considered the “frequency response”. This is because V_{in} carries information

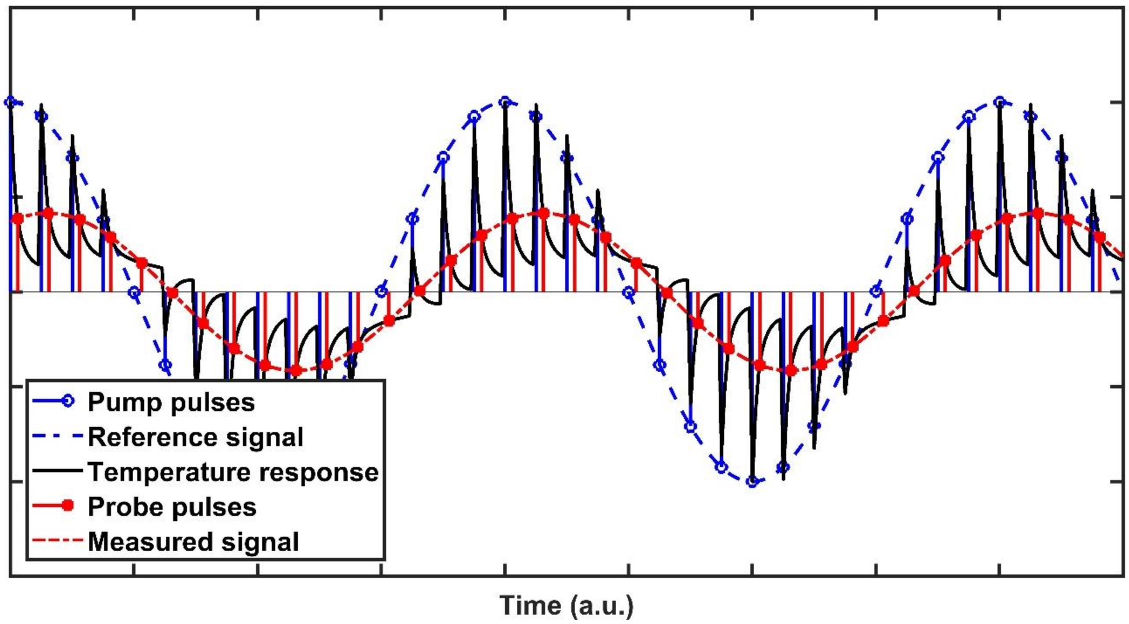

Figure 2.2. A representation of the modulated heating event and modulated response of the sample. The pump pulses incident on the sample are shown as blue stem open circles. The fundamental harmonic from the modulation of the pump beam is shown as a blue dashed line connecting the pump pulses. This results in the temperature response represented by a black solid line. Note that the temperature response is slightly shifted in phase. The probe pulses arrive at a later time delay and are shown as red stem solid circles. The lock-in amplifier detects a sinusoid, represented as a red dotted line, created by the modulated response of the probe beam due to the modulated temperature response of the sample.

reflecting the excitation and relaxation of the system due to a single pump pulse, while V_{out} holds information about the accumulation of multiple pump pulses on a longer time scale.[7, 14-15] For the work in this thesis, I will primarily focus on the impulse response (V_{in}); however, it is worth mentioning that the reason TDTR is so powerful is because both V_{in} and V_{out} can be used simultaneously to determine different thermal properties.[7, 14-15]

2.3 Analysis of a Spherical Nanofluid

In a TDTT measurement, there are several energy transport regimes.[27, 29, 35, 51-52] We will consider the case of a spherical nanoparticle in an optically transparent fluid.[11, 18-21] Initially, the pump pulse is absorbed by electrons in the nanoparticle, creating a population of hot electrons.[11, 18-21] The electronic system equilibrates within one picosecond.[11, 18-21] A nonequilibrium exists between electrons and vibrational modes in the nanoparticle, which lasts for several picoseconds.[11, 18-21] Finally, vibrational relaxation occurs from the nanoparticle into the surrounding fluid.[11, 18-21] It is this last regime that has been the focus of my work in this thesis. The thermotransmittance signal from the probe measures the change in the nanoparticle temperature in response to the heat input by the pump. In this section, I will derive the thermal response of a nanoparticle in a fluid by solving the heat diffusion equation.

The heat input from the pump is a function of the time varying power absorbed by the nanofluid and can be written as:[15-17, 53]

$$Q_{pu}(t) = A\,G(t) \tag{2.1}$$

where A is a constant representing an areal density [m^{-2}], $Q_{pu}(t)$ has units of [W m^{-2}] and $G(t)$ has units of [W] and has the form:[15-17, 53]

$$G(t) = \alpha E \exp(i\omega_{mod} t) \sum_{n=-\infty}^{+\infty} \delta(t - n\Gamma) \tag{2.2}$$

where α is the absorptivity of the nanofluid, E is the energy per pump pulse, ω_{mod} is the angular modulation frequency, and Γ is the time between pulses (12.5 ns). The summation is to account for the effect of individual pulses of the pump beam. We consider the heat diffusion equation in spherical coordinates for a spherically symmetric system as shown in

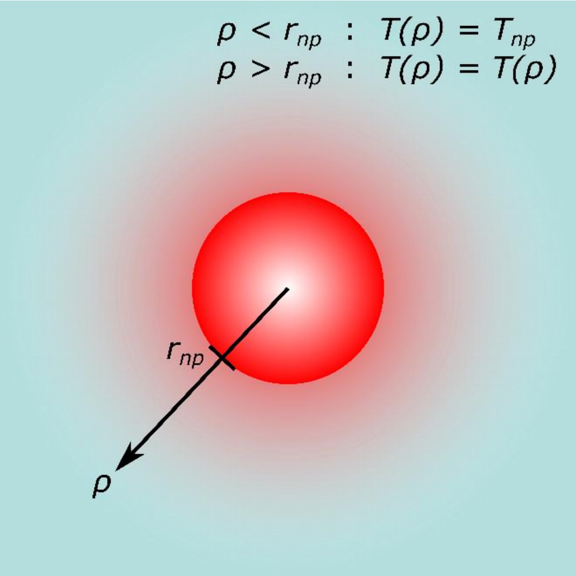

Figure 2.3. A spherical nanoparticle of radius r_{np} in a fluid. The nanoparticle is colored red and the fluid is colored light blue. At any given time, the temperature within the nanoparticle is spatially constant. For radial distances greater than the nanoparticle radius, there exists a temperature gradient due to the diffusion of heat from the nanoparticle into the fluid.

Figure 2.3. In this scenario, the nanoparticle is small enough that we may assume that the thermal gradient within the particle is negligible.[26-27, 29, 36] However, in the fluid there is a spherically symmetric thermal gradient.[26-27, 29, 36] We will first determine the temperature field in the fluid.

In the time domain, the spherical heat equation with spherical symmetry is given by:[54-55]

$$D\left(\frac{\partial^2 T(\rho,t)}{\partial \rho^2} + \frac{2}{\rho}\frac{\partial T(\rho,t)}{\partial \rho}\right) = \frac{\partial T(\rho,t)}{\partial t} \tag{2.3}$$

where D is the thermal diffusivity of the fluid, $T(\rho,t)$ is temperature, ρ is the spherical spatial coordinate, and t is time. It is mathematically convenient to write this in terms of the product $\theta(\rho,t) = T(\rho,t)\rho$:[54-55]

$$D\frac{\partial^2\theta(\rho,t)}{\partial\rho^2}=\frac{\partial\theta(\rho,t)}{\partial t} \tag{2.4}$$

A straightforward solution to this partial differential equation is found by first taking the Laplace transform to switch from the time domain to the frequency domain:[54-55]

$$D\frac{\partial^2\tilde{\theta}(\rho,\omega)}{\partial\rho^2}=i\omega\tilde{\theta}(\rho,\omega) \tag{2.5}$$

The tilde symbol "~" on top of a variable will be used to denote functions that have been transformed to the frequency domain via a Laplace transform $\tilde{y}=\mathcal{L}\{y(t)\}$. Now we define:

$$q^2=i\omega/D \tag{2.6}$$

and rearrange the heat equation:

$$\frac{\partial^2\tilde{\theta}(\rho,\omega)}{\partial\rho^2}=q^2\tilde{\theta}(\rho,\omega) \tag{2.7}$$

which has a solution of the form:[54-55]

$$\tilde{\theta}(\rho,\omega)=a\exp(q\rho)+b\exp(-q\rho) \tag{2.8}$$

where a and b are constants. We can immediately determine that $a=0$ because the solution is physically limited to finite temperatures in the limit that ρ approaches infinity. We impose the boundary condition that the fluid approaches temperature $\tilde{T}_f(\omega)$ on the fluid side of the nanoparticle/fluid interface:

$$\tilde{\theta}\left(\rho=r_{np}^{+},\omega\right)=\tilde{T}_f(\omega)r_{np}=b\exp\left(-qr_{np}\right) \tag{2.9}$$

where r_{np}^{+} denotes the fluid side of the interface. We can now determine b:

$$b=\tilde{T}_f(\omega)r_{np}\exp\left(qr_{np}\right) \tag{2.10}$$

and the solution for the temperature field in the fluid:

$$\tilde{\theta}(\rho,\omega)=\tilde{T}_f(\omega)r_{np}\exp\left(qr_{np}\right)\exp(-q\rho) \tag{2.11}$$

Rearranging this equation and separating the product $\tilde{\theta}(\rho,\omega) = \tilde{T}(\rho,\omega)\rho$ yields:[27, 29]

$$\tilde{T}(\rho > r_{np}, \omega) = \frac{\tilde{T}_f(\omega) r_{np}}{\rho} \exp\left(-q(\rho - r_{np})\right) \tag{2.12}$$

We now apply an energy balance to the energy stored in the nanoparticle, the energy lost to the surrounding fluid, and the energy absorbed from the pump in order to relate $\tilde{T}_f(\omega)$ to the temperature of the nanoparticle $\tilde{T}_{np}(\omega)$:[27, 29]

$$i\omega \frac{4\pi}{3} r_{np}^3 C_{np} \tilde{T}_{np}(\omega) + 4\pi r_{np}^2 \tilde{Q}_{BD} - \tilde{Q}_{pu}(\omega) = 0 \tag{2.13}$$

where C_{np} is the heat capacity of the nanoparticle, $\tilde{Q}_{BD}$ is the heat flux across the nanoparticle/fluid interface, and $\tilde{Q}_{pu}(\omega)$ is the transformed heat input from the pump given by:[15-17, 53]

$$\tilde{Q}_{pu}(\omega) = A\, \tilde{G}(\omega) = A\, \frac{2\pi\alpha E}{\Gamma} \sum_{n=-\infty}^{+\infty} \delta(\omega - \omega_{mod} - n\omega_{rep}) \tag{2.14}$$

where ω_{rep} is the angular repetition frequency of the Ti:Sapphire laser. The heat flux across the nanoparticle/fluid interface is defined as:[27, 29]

$$\tilde{Q}_{BD} = h_K \left(\tilde{T}_{np}(\omega) - \tilde{T}_f(\omega)\right) \tag{2.15}$$

where h_K is the thermal boundary conductance of the nanoparticle/fluid interface. Continuity of the heat flux in the fluid requires:[27, 29]

$$\tilde{Q}_{BD} = -\kappa_f \left.\frac{d\tilde{T}(\rho,\omega)}{d\rho}\right|_{\rho = r_{np}^+} \tag{2.16}$$

where κ_f is the thermal conductivity of the fluid. Taking the derivative of our solution for the temperature field in the fluid with respect to ρ at $\rho = r_{np}$ yields:[27, 29]

$$r_{np}\tilde{Q}_{BD} = \tilde{T}_f(\omega)(1 + q r_{np})\kappa_f \tag{2.17}$$

We now have three equations at our disposal to write an expression for $\tilde{T}_{np}$ in terms of materials properties and the heat input from the pump:

$$\tilde{T}_{np}(\omega) = \frac{\tilde{Q}_{pu}(\omega)}{\left[\left(i\omega\frac{4\pi}{3}r_{np}^{3}C_{np}\right) + \left(4\pi r_{np}^{2}h_{K}\left(1 - \frac{r_{np}h_{K}}{r_{np}h_{K} + (1 + qr_{np})\kappa_{f}}\right)\right)\right]} \qquad (2.18)$$

The in-phase signal $V_{in}(t)$ in the time domain is retrieved by taking the inverse Laplace transform which requires summing over the pump pulses or , equivalently, over all complex thermal wavelengths $1/q$:[27, 29]

$$V_{in}(t) = A\sum_{q=-\infty}^{+\infty}\left(\tilde{T}_{np}\left(\frac{q}{\Gamma} + \omega_{mod}\right) + \tilde{T}_{np}\left(\frac{q}{\Gamma} - \omega_{mod}\right)\right)\exp\left(\frac{i2\pi tq}{\Gamma}\right) \qquad (2.19)$$

where the constant A has been pulled out front and practically is used as a scaling factor.

2.4 Sources of Error

Alignment and collimation are decidedly important to the accuracy of a TDTT measurement. Our setup uses mirrors and irises liberally for facile and consistent alignment. As mentioned above, a beam profiler is used to measure the pump and probe spot radii which are typically ~20 and 10 μm, respectively. These large spot sizes have the benefit of minimizing the effects of varying spot size or shape. Further, even though these spot sizes are large, the high output power of our Ti:Sapphire laser allows us to maintain a substantial fluence. Variation in the in-phase signal (V_{in}) with no heating by the pump is on the order of ~0.1 μV while the measured V_{in} during measurements range from ~1 to 100 μV, depending on the powers used and material properties of the sample. This is a SNR greater than 10 and usually much higher.

The variation in V_{in} comes from several sources of noise. While some sources are unavoidable, such as Johnson and shot noise,[56] others can be strategically minimized. The principle noise source is electronic $1/f$ noise, which is a spectral noise distribution arising from fluctuations in the probe intensity around the reference frequency as detected by the lock-in amplifier.[57] As the name suggests, $1/f$ noise is inversely proportional to frequency.[57] Thus, a high modulation frequency of 10 MHz will have a much lower noise floor than a modulation frequency of 1 MHz. Note, 1 MHz measurements are certainly possible and the SNR can be improved by using a slower lock-in time constant to reduce the measurement bandwidth. The upper limit to the modulation frequency is determined by the repetition rate of the laser ($f_{mod} \leq f_{rep}/2$).[58]

Radio frequency (RF) noise is caused by external RF sources which can be picked up due to the antenna-like nature of Bayonet Neill-Concelman (BNC) cables, causing an added offset to the measured signal.[59] Furthermore, any objects that move into proximity of the BNC cables can change the surrounding electro-magnetic field and change this offset.[59] A simple solution to this issue is create an RF choke by winding the BNC cables around a ferrite toroid.[59] This effectively creates an inductor which blocks high frequency signals from RF interference (~5 MHz and higher).[59] Any remaining RF noise and other DC offsets can be subtracted from the lock-in signal before a measurement is made as long as they are constant.

Lastly, optical noise is also of concern, especially in systems that use the same wavelength for both the pump and probe beams. Because the modulation of the pump is so strong compared to the probe, and scattered pump light entering the photodetector will overwhelm the signal. However, this is easily avoidable in our two-color setup using a blue filter to remove the pump before the photodetector. Scattered pump light can be taken into account by making a measurement with the probe beam blocked and subtracting this from a normal measurement.

Chapter 3

Thermal Transport in Fullerene Solutions

3.1 Background

Since their discovery in the 1980s,[60] fullerenes and fullerene derivatives have been studied for their superior structural, chemical and transport properties, leading to applications in a range of fields including thermoelectric[61-65] and photovoltaic[66-71] devices, chemical storage and synthesis,[72-75] medicine,[74-78] and nanomechanical devices,[79-81] to name a few. Despite this potential, fullerenes have been far surpassed for (electronic) device applications by their allotropic relatives, carbon nanotubes and graphene, both of which can be found in industrial products.[82] The principal application of fullerenes has been as an n-type semiconductor for organic photovoltaics research, primarily employing the fullerene derivative [6,6]-phenyl C_{61} butyric acid methyl ester (PCBM).[66-67, 69-70, 83-86] Recently, it was discovered that PCBM displays an unparalleled, ultra-low thermal conductivity for a condensed solid, a remarkable 0.03 – 0.06 W m^{-1} K^{-1} at room temperature.[87-89] This desirable property provides an exciting trajectory for fullerene-based materials, opening the door for thermal management and thermal-based devices, *e.g.*, thermoelectric materials, thermionics, and nanoscale thermal barrier coatings. The origin of this further reduction of PCBM over bare C_{60} (factor of 2-3 lower thermal conductivity) is thought to be due to the localization of vibrational energy caused by the attachment of the functional group.[88-91] Thus, understanding the energetic relaxation mechanisms in fullerene derivatives and across their interfaces is of critical importance in order to understand the physical basis underlying their thermal transport properties.

To better understand these thermal transport pathways, the relaxation of photo-excited fullerenes and the resulting characterization of their relaxation processes and thermal transport properties have been the focus of considerable research in the last decade.[26, 88-89, 91-95] The thermal transport processes in fullerene derivatives, which here we define as C_{60} with molecular functional groups, have received far less attention. The vibrations contributing to the thermal transport properties of fullerenes consist of predominantly localized modes (commonly referred to as Einstein oscillations),[96] which been ascribed as the primary mechanism responsible for the ultra-low thermal conductivities observed in fullerene and fullerene-derivative thin films.[88-91] The interplay between these localized modes in energy exchange with a liquid environment is the focus of this report; specifically, we aim to answer the question: how do functional groups alter the thermal relaxation of excited fullerene derivatives into liquid surroundings? Understanding how fullerene derivative structures affect the vibrational mode coupling across molecular-based interfaces yields fundamental insight into the energy transport mechanisms in fullerene derivatives. Furthermore, this study advances the physical insight into heat transport across solid/liquid interfaces, elucidating the role of vibrational states of functional groups that affect thermal boundary conductance (h_K).

The vibrational coupling driving h_K has been extensively studied and is influenced by the material properties of the solids comprising the interface as well as the interfacial properties.[5] For example, h_K has been experimentally controlled *via* roughness,[97-99] interfacial mixing,[100-101] impurities,[102-104] and chemical bonding.[105-111] Most works involving chemical bonding observe no relationship between the characteristics of the molecule and the interfacial conductance, suggesting that thermal transport in the molecule itself is ballistic. Gaskins *et al.* has previously shown that the addition of henicosafluorododecyl-phosphonic acid (F21PA) molecules between various metals and sapphire results in a 40% reduction in h_K compared to the addition of other phosphonic acid molecules and the same interface without phosphonic acid molecules.[106] In other words, thermal transport across the F21PA molecules is not ballistic, and the intrinsic vibrational properties of the molecule affects h_K. This work suggested that there are cases in which the spectral features in the vibrational density of states (VDOS) of an interfacial molecular layer can be exploited to manipulate h_K. More specifically, when thermal transport in a molecule is diffusive, chemical functionalization can be used to tailor the vibrational modes available to conduct heat from one material to another.

The addition of molecules at interfaces can also serve to impact the bonding environment, which ultimately affects h_K.[105-111] At solid/liquid interfaces, chemical bonding has been shown, both experimentally[112-115] and with molecular dynamics (MD) simulations,[116-118] to alter h_K *via* the coupling of low frequency modes. The addition of an interfacial layer of molecules can affect the local VDOS near the interface but thermal transport within the molecule may still be ballistic. Contrastingly, as mentioned above, Gaskins *et al*. demonstrated diffusive transport across the molecular layers where the intrinsic vibrational properties of the molecule provide a distinct channel for heat conduction.[106] In this regard, studies of mode coupling due to chemical moieties at fullerene derivative/liquid interfaces has been limited to simulations.[94-95] Due to the results of these simulations[94-95] and the previous experimental work from Gaskins *et al*.,[106] we expect thermal transport in fullerene derivatives to be diffusive (*i.e.*, the vibrational modes in the functional group are thermally activated) and hypothesize that h_K is dictated by the presence of specific low frequency vibrational modes.

In this work, we conduct transient absorption measurements in dilute fullerene derivative solutions, measuring the relaxation pathways with picosecond resolution. Based on the temporal relaxation of the excited fullerenes, we determine h_K between the fullerene derivative molecules and the surrounding liquid, which, for the various molecules studies here, range from ~13 to 63 MW m^{-2} K^{-1}, depending on the structure and size of the functional group. We show a strong correlation between the increase in density of states of low frequency vibrations in the fullerene derivatives, which depends on the vibrational modes contributed by the functional group, and the aforementioned increase in h_K across the fullerene derivative and the liquid. More specifically, the presence and population of low frequency modes in the fullerene molecules (*i.e.*, those below ~6 THz) dictate the conductance of vibrational energy into the surrounding liquid. In this context, the phenyl-ester functional groups (which are terminated with alkane chains) show a strong increase in h_K with increasing chain length, suggesting the evidence of diffusive scattering in the functional moiety of these fullerene molecules. Furthermore, consistent with previous simulations showing low frequency modes directly coupling to the liquid,[94-95] our results suggest the enhancement in low frequency vibrations due to the addition of functional groups increases the direct coupling of vibrations from the molecules to the liquid environment, creating an additional pathway for heat conduction across the fullerene/liquid interface. Moreover, measurements on indene-functionalized fullerenes do not show an enhancement in h_K compared to a non-functionalized fullerene (C_{60}). This can be attributed to the fact that indene-functionalized fullerenes do not exhibit as large of a low frequency mode enhancement relative to bare C_{60} as compared to the phenyl-ester moieties, which further supports our conclusions regarding low frequency mode coupling of the molecules directly to the liquid as an additional pathway for heat flow.

3.2 Fullerene Solutions

The solutions were composed of six different solutes, which were purchased from Sigma Aldrich in powder form, and chlorobenzene and *ortho*-dichlorobenzene (ODCB) as a solvent (Figure 3.1). The thermal conductivities of the solvents are both ~0.125 W m^{-1} K^{-1} (Ref. [119]). We used an optically transparent solvent to make dilute fullerene solutions ensuring that our experiment is most sensitive to the transient absorption of singular fullerene molecules. Solutes included C_{60}, indene-C_{60} monoadduct (ICMA), indene-C_{60} bisadduct (ICBA), [6,6]-phenyl C_{61} butyric acid methyl ester PCBM, [6,6]-phenyl C_{61} butyric acid butyl ester (PCBB), and [6,6]-phenyl C_{61} butyric acid octyl ester (PCBO). All solutions were prepared at concentrations of 0.2 mM, at which we can assume monodispersity; that is, no aggregates are formed. At this concentration, the fullerene molecules are monodispersed yet the concentration is high enough to absorb a detectable amount of light for our pump-probe experiment. We measure the change in absorption *via* the time domain thermotransmittance (TDTT) approach.[13, 17, 26, 29, 35, 120]

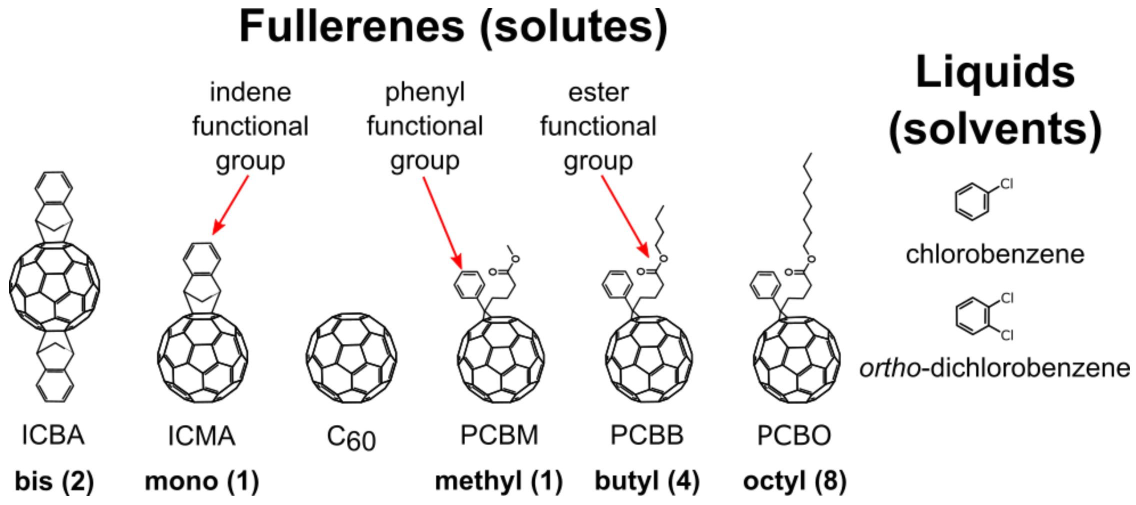

Figure 3.1. Samples in this study were 0.2 mM solutions composed of one of six different fullerene derivatives as the solute and one of two organic liquids as the solvent. Fullerenes include bare C_{60}, indene-functionalized buckyballs indene-C_{60} monoadduct and bisadduct (ICMA and ICBA), and phenyl-ester-functionalized buckyballs [6,6]-phenyl C_{61} butyric acid methyl ester, butyl ester, and octyl ester (PCBM, PCBB, and PCBO). Liquids include chlorobenzene (CB) and *ortho*-dichlorobenzene (ODCB).

In our analysis, we assume that the fullerene molecules are not influenced by each other and no aggregates are formed. To justify this assumption we perform our thermal measurements at several concentrations (1 mM, 0.2 mM and 0.05 mM). It should be noted that Huxtable *et al.* measured 1 mM solutions of higher order fullerenes in toluene after vigorous centrifugation and found no difference in optical density between the supernatant and the original suspension.[26] Since functionalization generally increases the solubility of fullerenes[74, 121-123] and fullerenes have higher solubilities in 1,2-dichlorobenzene (ODCB),[72, 121-122] we test the least soluble case, bare C_{60} in chlorobenzene, which has a solubility, S, of 6.35 mg/mL.[121-122] We find that the relaxation times are the same for concentrations of 0.05 mM and 0.2 mM but not 1.0 mM, indicating that 0.2 mM solutions are sufficient to avoid aggregation effects. Again, functionalized fullerenes have higher solubilities (*e.g.*, PCBM in chlorobenzene, S = 45 mg/mL),[121-122] as do fullerenes in ODCB (*e.g.*, C_{60} in ODCB, S = 22.9 mg/mL).[121-122] Thus, we are confident that our assumption of monodispersity is justified for all of the solutions examined here.

3.3 Relaxation Time Measurements

We monitor the change in absorption *via* a time domain thermotransmittance (TDTT) approach described in Chapter 2. The change in transmissivity of the probe beam at the frequency of the modulated heating event is monitored using a lock-in amplifier. The in-phase signal from the lock-in amplifier is representative of the impulse-response of the sample, i.e., the excitation and relaxation following pump pulse absorption.[17] Absorption of photons in organic molecules is driven by conjugated π-electrons.[124] At wavelengths of 400 nm and above, the widely accepted Woodward-Fieser rules[125-126] exclude the chlorobenzene and *ortho*-dichlorobenzene molecules that compose the liquid and the functional groups on C_{60} as sources of absorption. Thus, we can assume that the π-electrons within the buckyballs themselves are the absorbing agents in our solutions. Pumped electrons occupy excited states which relax *via* radiative (photon emission) and nonradiative (vibration coupling) processes.[127] Ultrafast pump-probe experiments show electron-vibration coupling occurs on sub-picosecond time scales while excited singlet and triplet lifetimes are on the order of nanoseconds and microseconds, respectively, and are dependent on the functionalization of C_{60} and the solvent.[127] Therefore, this suggests that the relaxation we observe during our TDTT measurements are indicative of a vibrational relaxation, as shown in previous works.[26, 94-95] Beam powers and spot diameters used were 30 mW at 40 µm and 15 mW at 25 µm for the pump and probe, respectively. We observe the excitation of fullerene molecules in solution due to the absorption of photons from pump pulses followed by their relaxation for up to 5.5 ns after excitation.

Example data from a TDTT measurement is shown in Figure 3.2. The initial peak is the excitation of fullerene electrons due to absorption of the pump pulse. Electrons equilibrate amongst themselves in the first few picoseconds (note, this is not recombination, as recombination rates are on the order of nanoseconds or longer).[127-134] The following vibrational relaxation (cooling) is the dominating effect observed as the decay of the TDTT signal for the next few hundred picoseconds. This thermal relaxation rate has been measured experimentally and computationally for higher order fullerenes, and ranges from ~10 to 200 ps with a strong dependence on functionalization.[26, 94-95] Although a complete analytical solution to the heat diffusion equation derived in the previous chapter can be applied to the data, a much simpler approach stemming from an analysis of the dominating thermal resistor was used here. More details are given in the next section. We normalize the in-phase signal at a time delay of 10 ps and fit the experimental data with a biexponential decay function

$$f(t) = A_1 \exp(-t/\tau_1) + A_2 \exp(-t/\tau_2) + A_3 \qquad (3.1)$$

at times t > 10 ps, where the first term is used to model the vibrational relaxation, the second to capture electronic effects, and the third is to account for the background (or baseline) absorbance. An example of the raw data (main figure) and model fit (inset) are shown in Figure 3.2. The resulting time constants for the vibrational and electronic terms are shown in Figure 3.3. Notice that the electronic time constant is dependent on the pump fluence. This is indicative of an electronic process, specifically depletion of the ground state. We do not see this dependence on the vibrational time constant, which provides

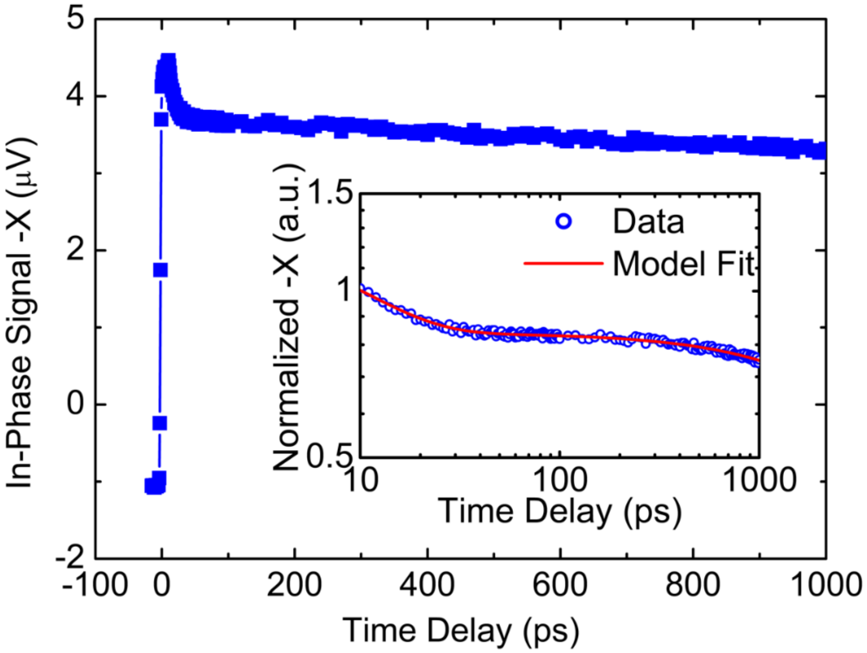

Figure 3.2. The main figure shows the raw data from a TDTT scan on the PCBM/ODCB solution. After the initial pump excitation, we observe biexponential behavior, a fast relaxation followed by a slow one. We normalize the data after the initial peak (~10 ps) and fit a biexponential decay curve. The inset shows the normalized data (open circles) with the biexponential model function (solid line). The measured signal continues to relax at a constant rate for the remainder of the TDTT scan (out to 5.5 ns, not shown).

further evidence that the measured relaxation times are representative of a vibrational process.

3.4 Analysis of Thermal Boundary Conductance

We can gain an understanding of the dominant thermal resistor in a nanofluid by considering a system controlled by the thermal boundary conductance h_K and a system controlled by the thermal effusivity of the fluid $\kappa_f C_f$.[26-27, 29] In the latter case, we assume

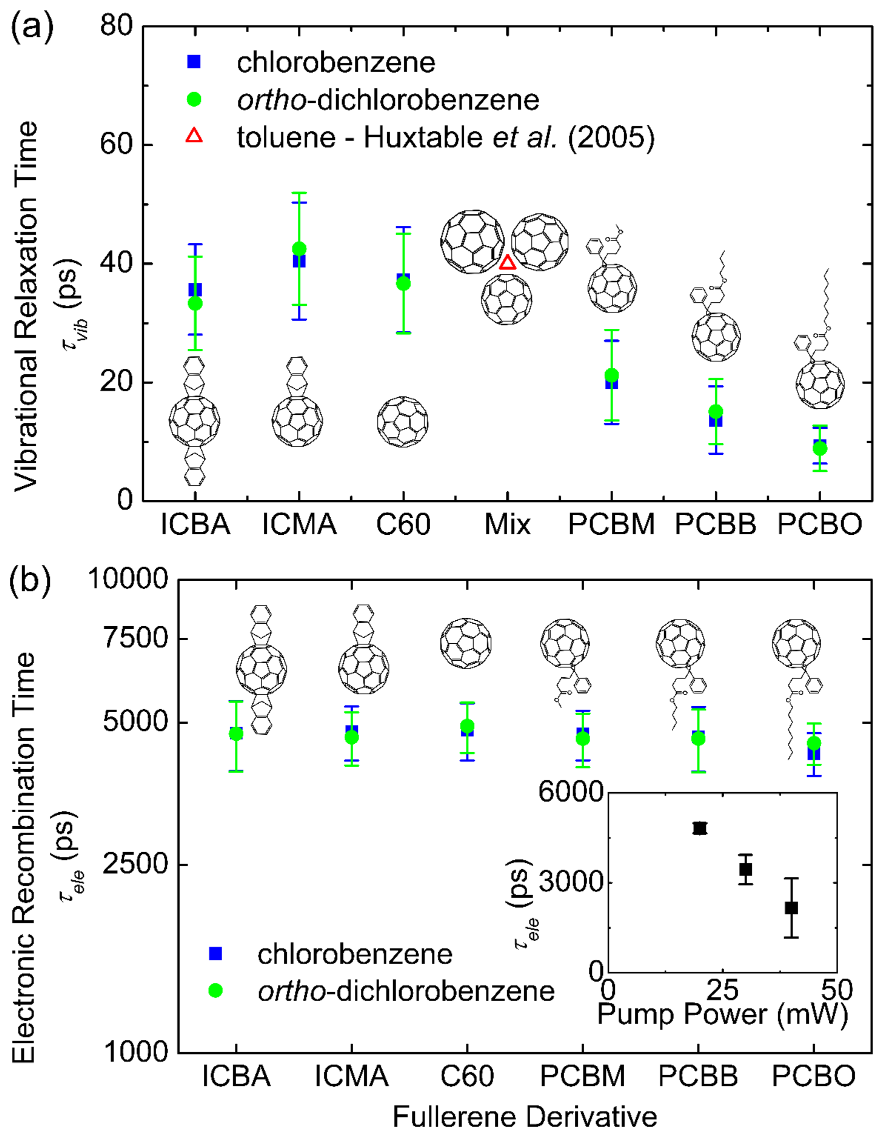

Figure 3.3. The second time constant corresponds to an electronic recombination time. The inset here shows the measured relaxation time as a function of pump power for which we observe an inverse relationship. We do not observe a dependence on solvent.

$h_K \rightarrow \infty$ and the relaxation time of the nanoparticle τ_d can be found by equating the energy of the nanoparticle $C_{np}V$ to energy of the surrounding fluid $C_f V$, where the control volume, V, of the surrounding fluid is defined within a thickness of the thermal diffusion length $l_d = \sqrt{D_f \tau_d}$ and $D_f = \kappa_f / C_f$ is the thermal diffusivity of the fluid. Thus we have:[26-27, 29]

$$\frac{4}{3}\pi r_{np}^3 C_{np} = 4\pi r_{np}^2 l_d C_f \tag{3.2}$$

where r_{np} is the radius of the nanoparticle. Inserting the defined thermal diffusion length and thermal diffusivity, we can solve for the relaxation time in the thermal effusivity controlled regime:

$$\tau_d = \frac{r_{np}^2 C_{np}^2}{9 C_f \kappa_f} \tag{3.3}$$

If the thermal boundary conductance is dominant, then the relaxation time of the nanoparticle τ_{BD} is found by equating energy stored in the nanoparticle to the energy transferred across the nanoparticle/fluid interface:[26-27, 29]

$$\frac{4}{3}\pi r_{np}^3 C_{np} = 4\pi r_{np}^2 h_K \tau_{BD} \tag{3.4}$$

and solving for the relaxation time τ_{BD} in the thermal boundary conductance controlled regime:

$$\tau_{BD} = \frac{r_{np} C_{np}}{3 h_K} \tag{3.5}$$

Now we can define a critical thermal boundary conductance $h_{K,C}$ by equating τ_d and τ_{BD}:[26-27, 29]

$$\frac{r_{np}^2 C_{np}^2}{9 C_f \kappa_f} = \frac{r_{np} C_{np}}{3 h_{K,C}} \tag{3.6}$$

and solving for $h_{K,C}$ yields

$$h_{K,C} = \frac{3 C_f \kappa_f}{r_{np} C_{np}} \tag{3.7}$$

The radius of a C_{60} molecule is ~3.58 Å.[26] Noting that the heat capacity of C_{60} (Ref. [135]) can be approximated as that of graphite at room temperature,[136] we find a volumetric heat

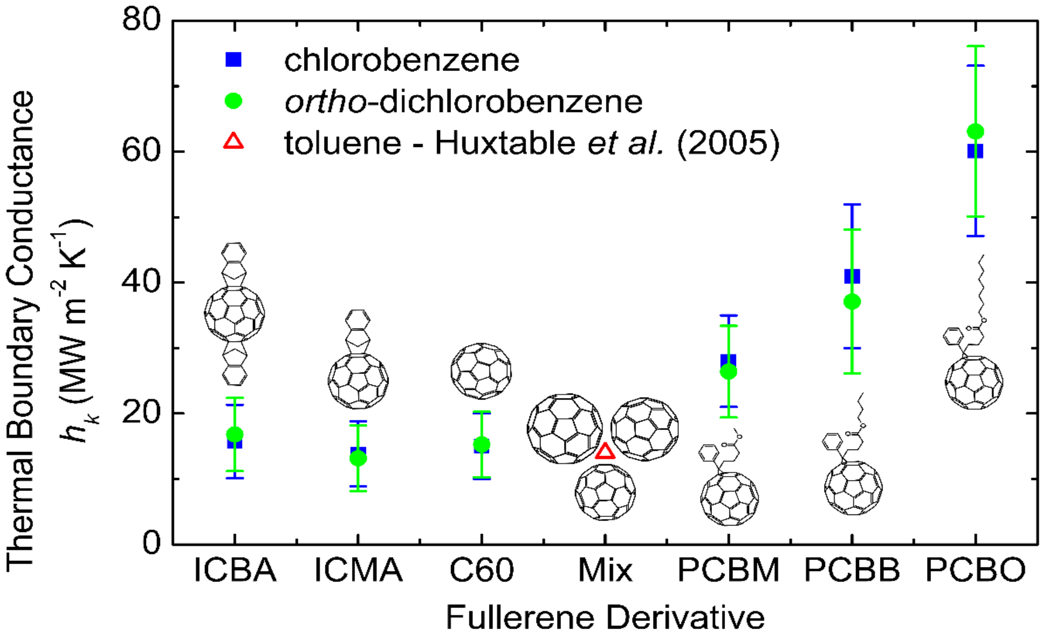

Figure 3.4. The effective thermal boundary conductance for each solution calculated using the equation $h_K = r_{np}C_{np}/3/\tau$. Blue squares represent chlorobenzene solutions, green circles represent *ortho*-dichlorobenzene solutions, and the red triangle represent toluene solutions of mixed higher order fullerenes from Huxtable *et al.* in 2005 (ref. [26]). Compared to C_{60} and other higher order fullerenes, indene-functionalized buckyballs show no statistically significant change in thermal boundary conductance while phenyl-ester-functionalized buckyballs show an increase.

capacity of 1.24 x 10^6 J m^{-3} K^{-1}. Using the average properties our solvents (κ_f = 0.125 W m^{-1} K^{-1} and C_f = 1.4 x 10^6 J m^{-3} K^{-1})[119] yields a critical thermal boundary conductance of $h_{K,C}$ ~ 1200 x 10^6 W m^{-2} K^{-1}. Since we expect values on the order of ~10 to 100 x 10^6 W m^{-2} K^{-1}, we assume that the thermal transport in this system is dictated by the thermal boundary conductance of the nanoparticle/fluid interface.[26] This means that we can calculate h_K directly from the fitted vibrational relaxation times using equation 3.5.

We observe a strong dependence of the first time constant on the structure and size of the functional group attached to the buckyball. The relaxation rate of a bare buckyball

(C_{60}) was determined to be 37±8 ps, resulting in h_K =15±5 MW m^{-2} K^{-1}. The fullerene derivatives with rigid ring structures (indene groups in ICMA and ICBA) relax similar to, or slightly slower than, a bare buckyball, resulting in a similar h_K; whereas those with flexible chain structures, such as the ester groups in PCBM, PCBB, and PCBO, relax more quickly with increasing chain length resulting in h_K as high as 63±13 MW m^{-2} K^{-1}, a four-fold increase compared to bare C_{60} (Figures 3.3 and 3.4). The second time constant, as shown in the Figure 3.3, showed no statistically significant dependence on the functional group or solvent; however, it varied inversely with the pump beam fluence, as would be expected for an electronic recombination process.[127]

Our measured vibrational relaxation times of bare C_{60} agree with the measurements of higher order fullerene mixtures by Huxtable *et al*.[26] within uncertainty. We believe our experiments have several distinct advantages of those of Huxtable *et al.* for interpretation of the results in the context of specific mode coupling across the fullerene/liquid interface. For one, their samples consist of a mixture of C_{84}, C_{78}, and C_{76} molecules, whereas our samples consist of pure (>97%) C_{60} derivatives, allowing us to isolate the effect molecular functional group has on our measurements. Second, Huxtable *et al.* used a single-color ($\lambda = 740$ to 800 nm) pump-probe setup while we use a two-color ($\lambda_{\text{pump}} = 400$ nm, $\lambda_{\text{probe}} = 800$ nm) setup, making it easy to separate and detect the probe signal. Lastly, fullerenes absorb an order of magnitude more in the 400 nm range,[129, 133] providing a signals due to increased pump absorption.

Our experimental measurements suggest that thermally active vibrational modes in the phenyl-ester chains can enhance the overall heat flow from the fullerene derivative to the liquid. The increase in the measured conductance *versus* length of the phenyl-ester chain points to the underlying diffusive vibrational thermal transport mechanisms in the functional moiety; specifically, scattering and thermalization of the vibrational modes increases the conductance due to the increased vibrational density of states (VDOS) of low frequency vibrations with increasing chain length – note, we would not expect a length dependence in the measured conductance if heat flow in the phenyl-ester chains was predominantly ballistic.

3.5 Comparison with Molecular Dynamics

To gain insight into the effect of functional groups on the relative spectrum of vibrational frequencies of an isolated C_{60} molecule, we compare our experimental results to VDOS generated from classical molecular dynamics (MD) simulations using the LAMMPS package[137] by Szwejkowski *et al.*.[36] The fullerene molecules (shown in Figure 3.1) and liquid toluene were simulated. The VDOS is proportional to the Fourier transform ($\mathcal{F}$) of the velocity autocorrelation function (VACF).[138] The velocity fluctuation time series was used to build the VACF of which the fast Fourier transform is computed. To compute the VDOS in units of counts per frequency per volume, the following equation is used:[139]

$$D(\nu) = \frac{1}{2} m \mathcal{F}(\mathrm{VACF}) \frac{1}{k_\mathrm{B} T} \rho \tag{3.8}$$

where m is the atomic mass, k_B is the Boltzmann constant, T is the local temperature, and ρ is the atomic density. Plots of the resulting VDOS for the fullerene derivatives considered in this work and liquid toluene are shown in Figure 3.5.

To test our hypothesis regarding the diffusive nature of thermal transport in fullerene derivatives and gain more insight into the vibrational mode coupling of functionalized fullerenes with liquids, we turn to molecular dynamics (MD) simulations to calculate the VDOS of each fullerene derivative molecule, along with liquid toluene as a representative benzene-based liquid. We only simulate liquid toluene for this work due to its established potential[140] and simulations procedures in previous works; furthermore, toluene has been used by Huxtable *et al.*[26] to study fullerene suspensions. The VDOS of chloro- and dichlorobenzene are expected to be similar to that of toluene which has a broad low frequency peak that extends to ~5 THz. In fact, due to the increased mass of chloro- and dichlorobenzene relative to toluene, we expect the vibrational states to be shifted to lower frequencies, which further supports our conclusion regarding low frequency coupling, found below.

A comparison of the VDOS of each of the fullerene derivatives and the liquid is shown in Figure 3.5. The gray dotted line denotes the maximum frequency of thermally activated modes at room temperature (estimated as $\nu_{300\ \mathrm{K}} = k_\mathrm{B}T/h$).[141] In general, functionalizing C_{60} creates an increase in the VDOS at low frequencies as compared to a bare buckyball. We focus our discussion on the low frequency range below 6 THz, as this frequency range drives the majority of the thermal conductance into the liquid at room temperature.[26, 94-95] As stated above, the fullerene derivatives have less intense but broader peaks compared to bare C_{60}. Most notably, the fullerene derivatives with ester groups (PCBM, PCBB, and PCBO) contain a broad near-zero peak whose shoulder extends out to ~3 THz. The fullerene derivatives with indene groups (ICMA and ICBA) also have distinct low-frequency peaks, albeit not nearly as broad as the ester-functionalized fullerenes.

ICMA has a peak near 1.3 THz while ICBA has two peaks near 1.2 and 1.4 THz. These differences can be explained by structural and chemical differences. The indene

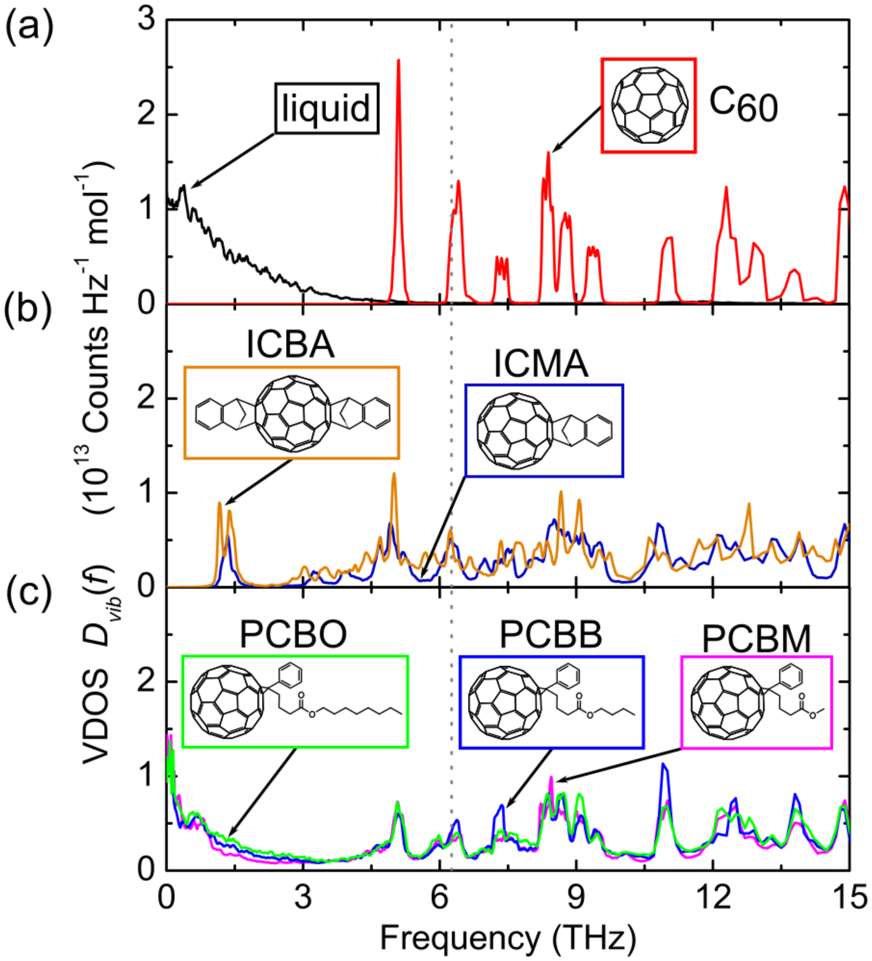

Figure 3.5. The vibrational density of states at room temperature calculated using MD are shown in panel (a) for liquid toluene (black) and C_{60} (red), in panel (b) for ICMA (navy) and ICBA (orange), and in panel (c) for PCBM (pink), PCBB (blue), and PCBO (green). The gray dotted line denotes the maximum frequency of thermally activated modes at room temperature assuming $\nu_{300\,\mathrm{K}} = k_{\mathrm{B}}T/h$, below this modes are gradually occupied according to Bose-Einstein distribution.[141] Simulations of bulk liquid toluene were assumed as a representative benzene-based liquid due to its well ascribed simulation parameters in previous works.

functional groups are more rigid due to the presence of stronger, shorter, double bonds and limited in their motion due to the bicyclic structure. In comparison to molecules with weaker, longer and single bonds, as found in the flaccid ester moiety, the rigidity of the indene functional group results in higher frequency vibrations. This, being the most notable difference between the VDOS of the different classes of fullerene derivatives (ring vs. soft chain structures), suggests that the presence or lack thereof of these low-frequency vibrational modes play a major role in determining the thermal transport efficiency from the fullerene molecule into the surrounding liquid. Again, the liquid supports heat conducting vibrational modes at frequencies below ~5 THz characterized by a broad near-zero peak in the VDOS.[26, 35, 142] Therefore, the vibrational modes in this range are expected to efficiently couple between the fullerene molecule and the liquid.

To quantify the role that these low-frequency modes play on thermal conductance, we calculate the accumulative internal energy and heat capacity that are given by

$$\alpha_U(\nu_{\text{cutoff}}) = \int_0^{\nu_{\text{cutoff}}} h\nu\, D(\nu)\, f_{\text{BE}}\, d\nu \tag{3.9}$$

and

$$\alpha_C(\nu_{\text{cutoff}}) = \int_0^{\nu_{\text{cutoff}}} h\nu\, D(\nu)\, \frac{\partial f_{\text{BE}}}{\partial T}\, d\nu \tag{3.10}$$

respectively, where ν_{cutoff} is the upper limit of the integral over linear frequency of which the accumulation is a function, $h\nu$ is the energy of a given vibration using Plank's constant, and $\frac{\partial f_{\text{BE}}}{\partial T}$ is the temperature derivative of the Bose-Einstein distribution. For equations (3.9) and (3.10), $D(\nu)$ is the unoccupied density of states, which we calculate by dividing the MD derived VDOS by the Maxwell-Boltzmann distribution. The internal energy of the molecule is related to the interfacial transmission coefficient, and the heat capacity is proportional to the intrinsic conductance of the molecule.[143-144] These functions are plotted in Figure 3.6. The VDOS of the liquid is also plotted to highlight the importance of the low frequency modes. We observe a substantial difference in the energy and heat capacity contained in the near-zero frequency modes of the phenyl-ester fullerenes and the ~1.3 THz

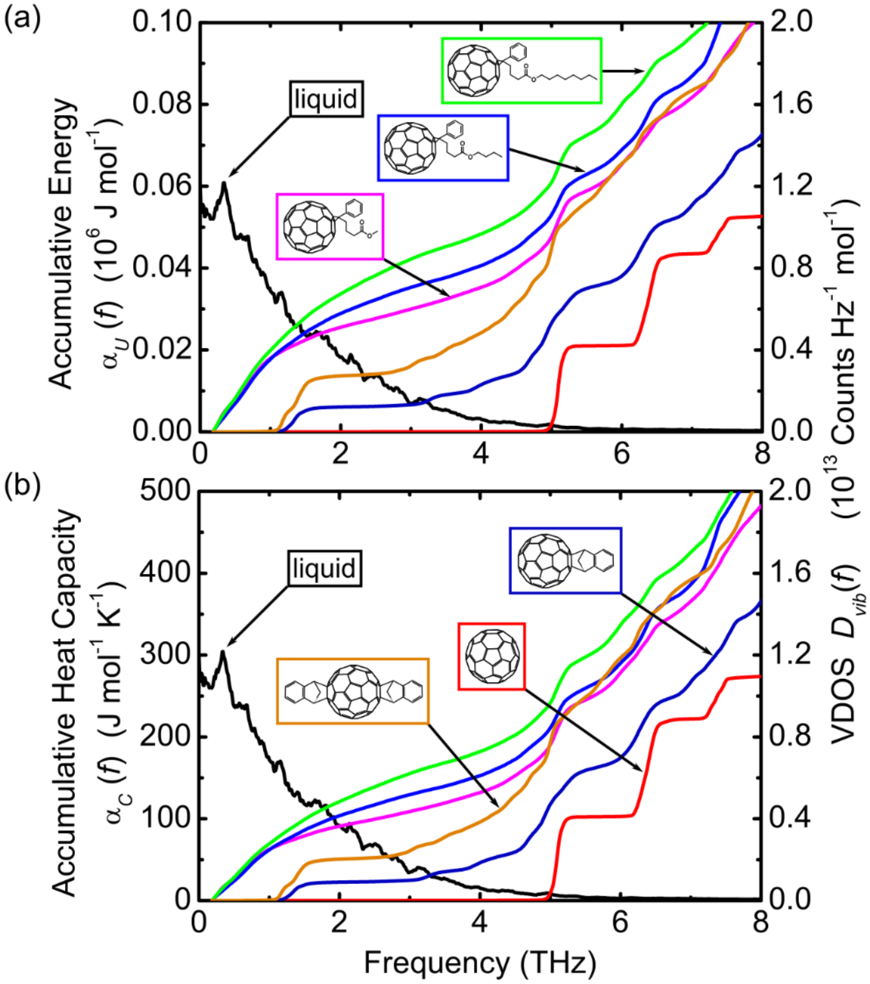

Figure 3.6. The accumulative energies and accumulative heat capacities as functions of linear frequency are plotted in panels (a) and (b), respectively, which include C_{60} (red), ICMA (navy), ICBA (orange), PCBM (pink), PCBB (blue), and PCBO (green). These correspond to the left y-axes. The vibrational density of states of the liquid is plotted in black in both panels and corresponds to the right y-axes. Simulations of bulk liquid toluene were assumed as a representative benzene-based liquid due to its well ascribed simulation parameters in previous works.

modes of the indene fullerenes. Furthermore, the lack of energy-storing modes in bare C_{60} below 5 THz is particularly notable. The accumulation functions for the phenyl-ester fullerenes begin to separate from each other around 2.5 THz in order of chain length, as might be expected. The accumulation functions of the indene fullerenes separate almost immediately due to the difference in the VDOS peaks around 1.3 THz. Above 5 THz we observe trends in the functionalized fullerenes that parallels the trends in bare C_{60}.

To expand on the above discussion, fullerene molecules interact with the surrounding liquid *via* van der Waals forces,[26, 94-95] which are associated with lower frequency vibrations. Similarly, liquid molecules interact with each other through vibrations in this same low frequency regime.[26, 94-95] Therefore, strong coupling from the fullerene molecule to the liquid occurs through these low-frequency modes.[26, 94-95] Thus, we expect thermal transport between the liquid and the fullerene to occur *via* the vibrational modes with frequencies within the first 5 THz, where the broad peak in the liquid VODS lies. Since there are a small number of low frequency modes in C_{60}, there is a small amount of overlap between the low frequency VDOS of the liquid and C_{60}, which results in a lower h_K as compared to functionalized C_{60} molecules. The functionalized fullerenes with the soft chain structures (PCBM, PCBB, PCBO) have a higher density of low frequency modes that can couple well with the liquid and, thus, have a higher h_K. While we expect a shift in the VDOS towards lower frequencies with an increase in molecular mass (*i.e.*, adding any molecule to C_{60} will create vibrations at lower frequencies), we do not observe the same effect for ICMA and ICBA, indicating that a shift in the vibrational modes due to a mass increase in the molecule is not the mechanism driving the increase in mode coupling across the fullerene/liquid interface. We therefore conclude that the increase in h_K in the soft chain fullerene derivatives as compared to the ring structures (or bare C_{60}) is due to the specific modes of vibrations intrinsic to the addition of the soft chain-like groups attached to PCBM, PCBB, and PCBO.

Qualitatively similar results were observed in the computational by Kim *et al.*[94] and Shenogin *et al.*.[95] Both extensively studied the effects of functionalization on thermal relaxation of C_{60} in liquid water and octane, respectively. Shenogin *et al.* analyzed the role of functionalizing alkane chain length and observed a decrease in thermal relaxation time (or an increase in conductance) with an increase in length.[95] Furthermore, the relaxation time is length independent beyond 10 CH_2 segments which was supported by the nearly constant steady state temperature of the chain beyond the 10th segment.[95] Alkane chains are qualitatively similar in their structure to the ester moieties in PCBM, PCBB, and PCBO. We observe the expected qualitatively similar trends in h_K from our experiments. We avoid generalizing these findings, as changing the concentration, solvent, or fullerene derivative may produce different experimental results.

3.6 Summary

Based on our accumulative internal energy and heat capacity calculations, we infer that the majority of differences in vibrational mode coupling between the fullerene molecules and the liquids liquid occur at low frequencies (below ~1.5 – 2 THz), where there are large number of vibrational states occupied in PCBM, PCBB, and PCBO but less so in ICMA, ICBA, and C_{60}. Thus, to enhance the heat transfer from a fullerene molecule to a liquid, functional groups with soft hydrocarbon chains should be used to populate this low frequency regime with vibrational modes. Our findings suggest that the functional groups can directly couple energy to the liquid as a parallel path of heat conduction beyond the low frequency vibrational modes in the buckyball itself. We are aware of only one other experimental work where the intrinsic vibrational properties of an interfacial molecular layer affects the total heat flow across interfaces.[106]

While we acknowledge that there is evidence of nonequilibrium between vibrational modes in the fullerene molecule,[26, 94-95, 113-114, 116-117] we limit our analysis to the determination of a single relaxation rate based on our experimental measurements. We do not attempt to make additional assumptions to deconvolve physical processes that could be occurring beyond the resolution of our experiments. Our experimental results clearly demonstrate that the fullerene derivative/liquid heat transfer rate is largely dictated by the low frequency vibrational modes of the fullerene molecule that overlap with those of the liquid. The effective h_K that results from this simple analysis lies in the broad applicability of this advance in interfacial physics. For example, knowing the energy exchange regardless of the vibrational mode is an essential knowledge for designing photothermal medical techniques and electronics or photovoltaic components. We have experimentally demonstrated a method for enhancing h_K between a buckyball and a liquid four-fold (from ~13 to 63 MW m^{-2} K^{-1}) based on chemical functionalization with soft chain-like groups, in which the addition of the molecular groups changes the vibrational nature of the molecule, and therefore enhances h_K. We note that nearly all previous works measuring h_K across functionalized interfaces have never observed the intrinsic vibrational properties of the molecular layer to affect heat flow. Rather, trends in h_K have been attributed to changes in bond energies driven by head- and tail-group interactions at the contacts. In fact, previous works have shown that heat flow through interfacial molecules is primarily ballistic. Our results demonstrate that the intrinsic vibrational modes of molecules at an interface can in fact lead to an increase in h_K due to a change in the overlap of the vibrational density of states of the two materials comprising the interface. We note that all of our experiments were performed at room temperature; future studies should consider temperature dependent measurements to gain additional insight into the effects of vibrational spectra on thermal boundary conductance.

Chapter 4

Thermo-optic Properties of Protein Aggregates

4.1 Background

All proteins are polymers made up of amino-acid monomers.[145] The arrangement of amino-acids is extremely specific and will determine the shape and function of the finished protein.[145] Proteins can be coarsely divided into two groups: globular and fibrous proteins.[145] Globular proteins have a complex folded shape and are water soluble.[145] Many globular proteins are used for transport, such as hemoglobin which transports oxygen in the blood stream.[145] Fibrous proteins have a simpler, thread-like shape and are insoluble in water.[145] Fibrous protein assemblies are often characterized by long-range-ordered molecular structures (e.g., β-sheets, coiled coils, triple helices) that arise due to repetitive amino-acid sequences and that impact function broadly.[145] These proteins are of high interest for materials engineering because of the role they play as structural materials (e.g. collagen and elastin).[145-146]

Advances in genetic recombination for protein synthesis have made it possible to create fibrous proteins whose properties can be engineered by specifying amino-acid sequences to create the desired higher order structures (e.g. β-sheets, coiled coils, triple helices).[42, 146-151] However, one of the most difficult problems in biology is predicting the structure of proteins based on their primary structure (amino-acid sequence).[152] Although homology modeling has been fairly successful for predicting globular protein structures, it is less well-suited for fibrous proteins.[153-154] Traditional techniques for probing protein structure include Fourier transform infrared spectroscopy (FTIR), circular dichroism (CD), dynamic light scattering (DLS), fluorescence spectroscopy, nuclear magnetic resonance (NMR), cryoelectron microscopy (cryo-EM), small-angle X-ray scattering (SAXS), and X-ray crystallography.[155] However, there remains an urgent need for fast and efficient techniques that can screen the properties of large numbers of protein sequences with minimal sample volume or in living cells.[156] In this chapter, I describe how time-domain thermotransmittance (TDTT) can be used for protein screening.

The protein aggregates in this study have a semi-crystalline morphology originating from crystalline β-sheet regions separated by amorphous regions (Figure 4.1).[42] Note, crystallinity here is similar to the concept of inorganic crystals in that there is long-range order and this can be measured using X-ray techniques.[155] Proteins with different degrees of crystallinity have different capabilities to dissipate heat and, thus, have different thermophysical properties (e.g. the thermo-optic coefficient).[42] In Chapter 1, I introduced the relationship between the thermotransmittance signal and the thermo-optic coefficient. As shown in this Chapter, the degree of crystallinity can be directly related to the thermo-optic coefficient, meaning it should be possible to distinguish the crystallinity of different protein aggregates (both films and *in vivo*) using TDTT. Moreover, a single TDTT measurement can be made in a matter of seconds, a feat that would be impossible to achieve with existing approaches such as fluorescence, immunostaining, or functional assays.[157]

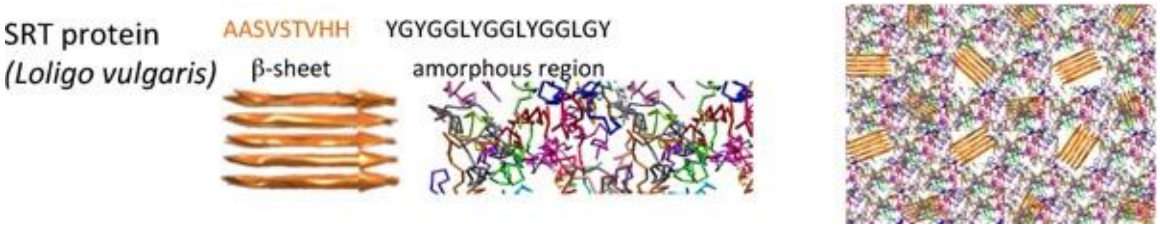

Figure 4.1. Computational model of SRT protein. Crystalline regions are formed from β-sheet structures which are separated by amorphous regions. Variations in the amino-acid sequence can change the size and order of the crystalline regions. This figure is from the previous work of our collaborators Demirel *et al*.[146]

4.2 Protein Films

In this work, I used TDTT to study the thermos-optic response of silk- and squid ring teeth-derived proteins. Silk[158] and squid ring teeth (SRT)[159] are semi-crystalline proteins that form flexible, biodegradable, and thermally and structurally stable materials. The semi-crystalline morphology of these proteins, which originates from their β-sheet secondary structures, enables genetic tuning of their physical properties (a computationally generated illustration of SRT proteins is shown in Figure 4.1).[42, 146-151] Silk and SRT protein complexes are composed of several proteins of varying molecular weight.[150] However, this heterogeneity renders variability in physical properties of such samples. Therefore, we also studied a recombinant SRT[149] protein ("Rec") with a unique molecular weight (i.e., 18 kDa) that forms a monodisperse sample. The sample fabrication and structural characterization are detailed in the previous works from our collaborator on this project, Dr. Melik Derirel from the Pennsylvania State University.[42, 146-151] These characterization techniques and the resulting properties are summarized in Table 4.1.

Table 4.1. Protein characterization results. The crystallinity index was calculated as the ratio of the area of crystal peaks to the total area by fitting the Lorentz-corrected WAXS intensity data using Gaussian functions. The amide-I band (1600–1700 cm^{-1}) measured using FTIR is representative of the secondary structures of the respective proteins. Based on the peak area, contribution of secondary structures is estimated below. The thermo-optic coefficient was previously measured using the resonance of whispering gallery mode (WGM) structures.[151]

	Silk	**SRT**	**Rec**	**m-SRT**
XRD[42]				
Crystallinity index X_c (%)	23	33	40	57
FTIR[42]				
β-sheet (%)	24	34	38	57
Random coil (%)	36	36	34	16
α-helix (%)	6	12	10	8
Turns (%)	34	18	18	19
WGM resonance[42, 151]				
Thermo-optic coefficient dn/dT (10^{-4} K^{-1})	-1.15	-4.28	-6.99	−6.40

The temperature dependence of the refractive indices (i.e., thermo-optic coefficient) of the proteins was reported earlier based on optical cavity measurements (Table 4.1).[151] In general, the thermo-optic coefficient can be written as a function of density change and temperature change,[7]

$$\frac{dn}{dT} = \left(\frac{\partial n}{\partial \rho}\right)_T \left(\frac{\partial \rho}{\partial T}\right) + \left(\frac{\partial n}{\partial T}\right)_\rho = -\rho \left(\frac{\partial n}{\partial \rho}\right)_T \alpha + \left(\frac{\partial n}{\partial T}\right)_\rho \qquad (4.1)$$

where ρ is the density and α is the coefficient of thermal expansion. The first term on the right side of the equation is the volume-dependent thermal response, which is related to thermal expansion. The second term, on the other hand, is the volume independent thermal response that is solely determined by the electronic structure of the material. The thermal expansion coefficients, α, for all protein samples ($-95 \times 10^{-6} \pm 7 \times 10^{-6}$ K^{-1} for SRT proteins and $-300 \times 10^{-6} \pm 10 \times 10^{-6}$ K^{-1} for silk) were measured previously.[151] Apparent negative thermal expansion coefficients are not surprising for structural proteins.[151, 160] For rubbery materials, the thermal expansion coefficient depends on the strain.[151, 160] In general, the total expansion is obtained by adding the expansion coefficient, α, to the unstressed material, $\alpha' = \alpha - \varepsilon/T$.[151, 160] For example, a natural rubber stretched three times of its length gives a contribution of about -10^{-2} K^{-1} at room temperature.[160] Similarly, silk shrinks significantly in size when hydrated due to inter-domain stresses (i.e., super-contraction of amorphous domains) in the native form.[161] For conventional polymers, the volume independent index change $\left(\frac{\partial n}{\partial T}\right)_\rho$ is small enough to be ignored.[162] Hence, Zhang et al.[162] showed a linear relationship between dn/dT and α values by ignoring the volume independent term for conventional polymers. The change in transmissivity measured with TDTT is directly related to the change in refractive index (i.e. $dTr/dT{\sim}dn/dT$) and has the same sign, assuming $n > 1$. The refractive index n was measured to be ~1.55.[151] Thus, the measured change in transmissivity is representative of the change in refractive index due to a change in temperature.

4.3 Thermotransmittance Measurements

I measured the changes in the ultrafast absorption properties due to changes in temperature using time-domain thermotransmittance (TDTT) (Figure 4.2). The probe spot size was 14 µm (1/e^2 diameter) with an average power of 4 mW. The pump spot size was 34 µm and the average pump power was varied to change the relative temperature rise in

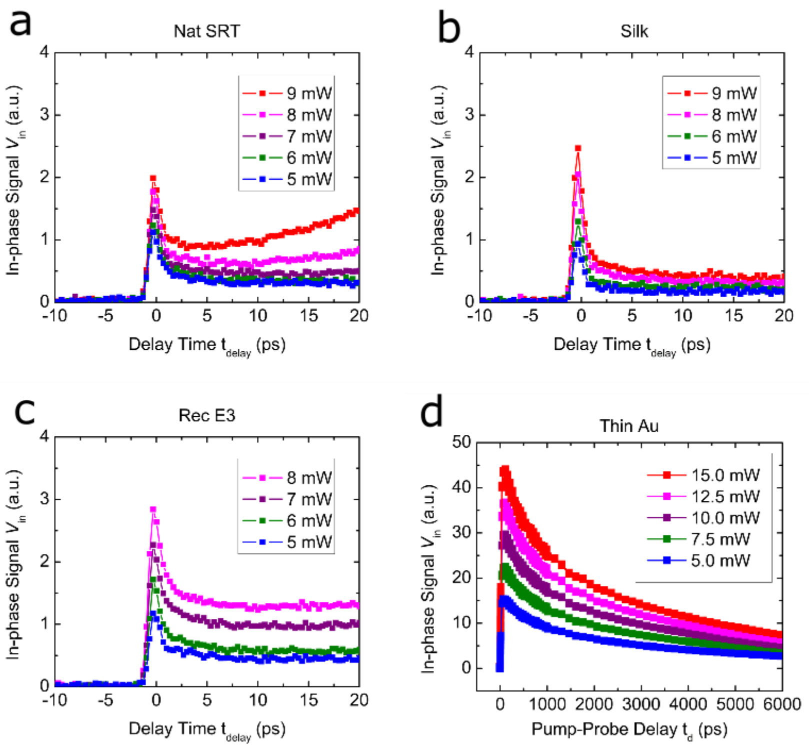

Figure 4.2. In-phase signal due to a heating event from a pump laser pulse as a function of the delay time between the pump and probe beams for native SRT (a), silk (b) and recombinant SRT (c) proteins. The measured change in transmissivity (dTr) at the different pump powers, which increases the per-pulse temperature rise, is representative of the change in refractive index due to a change in temperature (dn/dT). (d) Control experiment with Au thin film.

the samples during TDTT measurements. The amplitude modulation frequency of the pump was 8.8 MHz. The pump is used to trigger a rapid thermal process in the sample and the probe beam is used to examine the excited relaxation dynamics and energy changes of the excited volume. The temporal evolution of this process is monitored by varying the relative delay time between the pump and probe pulses. While the rapid absorption of the pump pulse leads to both temperature changes and thermal expansion, these signatures of the optical changes of the sample are separable in the time domain.[102] The characteristic signatures of the temporal thermal response are a rapid exponential decay in ~2 ps after laser absorption, representing nonequilibrium redistribution and coupling among thermal carriers, followed by a slower exponential decay, representing the change in the absorption of the sample that is linearly related to temperature (i.e., diffusive thermal transport).[15]

My measurements are performed outside the picosecond interval, which also ensures that the measurements avoid any non-linear optical effects from simultaneous pump and probe absorption in the sample. These TDTT measurements on three different proteins are then related to the volume independent term of the thermo-optic coefficient. The average in-phase value used for Figure 4.3 is calculated by averaging the normalized in-phase response of the transmission decay following pump excitation from pump-probe time delays of 5 to 20 picoseconds (Figure 4.2); these values are also used for calculation of the error bars. Monitoring the volume-independent thermotransmittance signal as a function of pump power shows linear relationships with distinct slopes for each of the different protein materials (Figure 4.3). These data are used to compute the thermo-transmission coefficient of each sample, which are related to the thermo-optic coefficients of the same materials (Figure 4.3).[151] We benchmark our measurements and analysis using a thin gold film (Figure 4.2), as the thermo-optic coefficients of gold films have been extensively characterized.[163]

Even though transient temperature rises are quite small, we observe long time heating effects after laser exposure time as little as 5 minutes which is most likely due to the accumulation of pulse energy from our 80 MHz oscillator. Figure 4.4 shows the in-phase signal at 20 ps pump-probe delay time as a function of lab time. Measurements reveal thermal runaway effects after only 5 minutes in recombinant (green upwards triangles) and native SRT (blue downwards triangles) but not silk (red circles). Silk is insensitive to these effects while native and recombinant SRT increase substantially with lab time. Because of

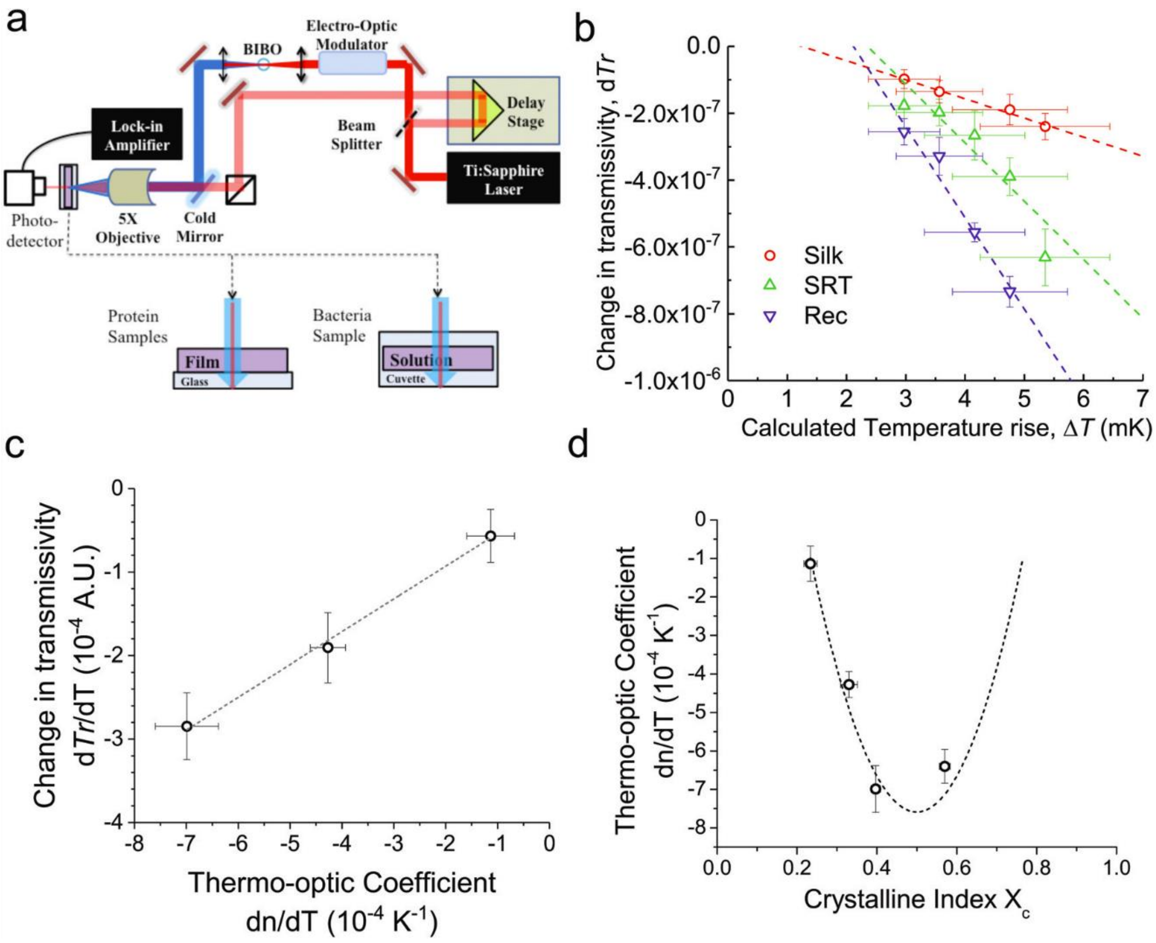

Figure 4.3. Transient thermo-optic set up and protein measurements. (a) Schematic of typical TDTT set up. The measured change in transmissivity is related to the change in refractive index due to a change in temperature. (b) Change in TDTT signal dTr as a function of normalized temperature rise induced from the ultrafast laser-heating event and measured via the 800 nm probe pulses. These data are related to dn/dT at 800 nm. The measured in-phase TDTT signal was averaged over the pump-probe delay time from 5 to 20 ps. The temperature rise induced from the pulsed heating was calculated via parabolic-one-step model for pulsed laser heating, assuming homogeneous absorption of the 400 nm pump light through the sample thickness. (c) The normalized thermotransmittance increases linearly with the thermo-optic coefficient. (d) Crystallinity index as a function of the thermo-optic coefficient is shown for four samples. Methanol treated SRT has increased crystallinity (e.g., X_c increased from 0.34 to 0.58). The dashed line shows theoretical prediction for thermo-optic coefficient (e.g., $\frac{dn}{dT} \sim [X_c(1 - X_c)]$) as a function of crystallinity.

this, we only consider measurements taken within 5 minutes to be representative of the intrinsic material properties we are interested in and must rely on measuring multiple spots on the sample to gather reliable data. All data reported in the manuscript were taken at less than 5 minutes exposure to the TDTT pump laser, ensuring minimal thermal runaway.

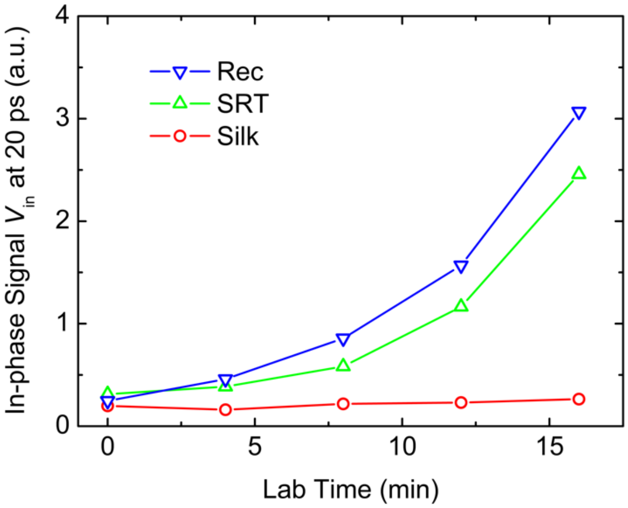

Figure 4.4. In-phase signal at 20 ps pump-probe delay time as a function of lab time. Measurements reveal thermal runaway effects after only 5 minutes in recombinant (green upwards triangles) and native SRT (blue downwards triangles) but not silk (red circles). All data reported in the manuscript were taken at less than 5 minutes exposure to the TDTT pump laser, ensuring minimal thermal runaway.

4.4 Analysis of Thermo-optic Coefficient

We wish to relate the measured thermotransmittance signals as functions of pump power to the crystallinity of the measured protein aggregates by connecting the two with expressions for the thermo-optic coefficient. We start with the Fresnel equation for the transmitted light Tr at normal incidence:[7]

$$Tr = \frac{4n}{(n+1)^2} \tag{4.2}$$

where n is the index of refraction. Taking the derivative with respect to n yields:

$$dTr = \frac{4(1-n)}{(n+1)^3} dn \tag{4.3}$$

where we have rearranged the equation by multiplying both sides by dn. It is already seen that the measured change in transmittance is directly proportional to the change in refractive index.

Beer's law is used to relate the absorbance of light A to the concentration c (or volume fraction) of the attenuating species:[164]

$$A = \epsilon\, c\, l \tag{4.4}$$

where ϵ is the absorbance coefficient and l is the optical path length. We can rewrite this equation in more convenient terms by recognizing three things. First, the absorbance is a logarithmic function of the changing light intensity $A = \ln(I_0/I)$ and thus $-A = dI/I = dTr$.[42, 164] Second, the concentration can be replaced by the product of volume fractions of the crystalline and amorphous species $\epsilon\, c = a\, \mathrm{X}_c \mathrm{X}_a = a\, \mathrm{X}_c(1-\mathrm{X}_c)$ where now the absorbance coefficient simply has different units.[164-165] Third, in anticipation of a substitution for the thermal expansion coefficient, we write the optical path length as z. These changes lead to the following expression:[42]

$$dTr = \frac{dI}{I} = -a\mathrm{X}_c(1-\mathrm{X}_c)dz \tag{4.5}$$

where X_c is the volume fraction of crystalline regions in (or crystallinity index of) the protein aggregate.

Combining the expressions derived from the Fresnel equation and Beer's law yields:[42]

$$\frac{4(n-1)}{(n+1)^3} dn = a\mathrm{X}_c(1-\mathrm{X}_c)dz \tag{4.6}$$

Dividing both sides by an infinitesimal change in temperature dT results in:[42]

$$\frac{4(n-1)}{(n+1)^3}\frac{dn}{dT} = a\mathrm{X}_c(1-\mathrm{X}_c)\frac{dz}{dT} \tag{4.7}$$

We can now substitute the thermal expansion coefficient $\alpha = \frac{1}{z}\frac{dz}{dT}$ into the equation to get:[42, 160]

$$\frac{4(n-1)}{(n+1)^3}\frac{dn}{dT} = a\mathrm{X}_c(1-\mathrm{X}_c)\alpha z \tag{4.8}$$

Finally, we rearrange the equation to reveal the relationship between the thermo-optic coefficient and the crystallinity index:[42]

$$\frac{dn}{dT} = az\frac{(n+1)^3}{4(n-1)}\mathrm{X}_c(1-\mathrm{X}_c)\alpha \tag{4.9}$$

This relationship is verified from previous measurements of the thermo-optic coefficient for these protein aggregates (Figure 4.3).[151]

We now have measurements of the thermotransmittance response of the protein aggregates as a function of pump power and an expression relating the thermo-optic coefficient to the crystallinity of the protein aggregates. Next, we seek to calculate the temperature rise due to absorption of the pump pulse. We start with an energy conservation equation for a single laser pulse as a thermal energy source and the protein film as a thermal energy storage medium:[42, 166]

$$C\frac{dT}{dt} = \frac{AF}{d\,t_p}\exp\left[-2.77\left(\frac{t-2t_p}{t_p}\right)^2\right] \tag{4.10}$$

where C is the volumetric heat capacity of the protein (~1.8x10^6 J m^{-3} K^{-1}),[20, 148, 167-168] AF is the absorbed laser fluence (~10% of incident pump), d is the thickness of the film

(~1 µm), and t_p is the laser pulse width (~200 fs). We calculate the absorption by measuring the laser power of the pump and probe beams before and after the sample and accounting for reflection from a glass substrate at normal incidence. The solution to this ordinary differential equation is:[42, 54, 166]

$$T(t) = \frac{AF}{Cd}\left[0.532 - 0.532\,\mathrm{erf}\left(3.33 - \frac{1.66t}{t_p}\right)\right] \tag{4.11}$$

where erf is the error function. Given the different pump powers used and the pump spot size, the temperature rise in the protein films was on the order of ~5 mK.

The average in-phase signal between 5 and 20 ps is plotted as a function of the calculated temperature rise in Figure 4.5 revealing distinct slopes for each of the different protein materials. These slopes are used as a “thermo-transmittance coefficient” of each sample, which are related to the thermo-optic coefficients of the same materials.[151] As shown Figure 4.5 they are linearly proportional to one another, as expected.[151] Plotting the thermo-transmittance coefficients calculated from the experimental data for the tested proteins as a function of crystallinity revealed that the thermo-optic coefficient becomes more negative with increasing crystallinity index of the protein up until a crystallinity index of 0.5 (Figure 4.4). This distinct trend allows for comparison (and potentially identification) of semi-crystalline proteins.

4.5 Summary

We report the development of a novel use of the TDTT technique to characterize the nanoscale morphology of structural proteins. We also show theoretically that the thermotransmittance measurement is correlated to the protein crystallinity via the thermo-optic coefficient. As shown here, time-resolved changes in the refractive index of semi-crystalline proteins vary as a function of temperature, and the strength of this effect correlates with crystallinity. Ultimately, this allows us to quantify rapidly the crystallinity of a protein sample using TDTT by decoupling volumetric thermal expansion from its structural response at room temperature. This approach can potentially be used for screening an ultra-large number of proteins *in vivo*. The size of the library for these proteins is simply limited by the fluidic and electronic components of the sorting since the TDTT technique operates in the order of minutes to seconds. If this screening technique is achieved, we could answer many fundamental questions in protein research, such as the underlying sequence–structure relationship for structural proteins. Successful development of this technique for proteins will have a significant impact on multiple applications in various fields (e.g., materials science, synthetic biology, metabolic engineering, agriculture, prion based diseases) and open new avenues of protein research.[169]

Chapter 5

Summary, Impact, and Future Projects

Optical pump-probe measurements are routinely performed in the field of nanoscale heat transfer. The last three decades have seen much progress in the characterization of technologically relevant material systems and in furthering our understanding of the fundamental mechanisms of thermal transport. The vast majority of measurements are implemented in a reflection geometry to measure the thermoreflectance signal; however, some material systems or thermophysical properties can be easily characterized using a transmission geometry. The work in this thesis represents a study on the adaptability of the time-domain thermotransmittance (TDTT) technique, particularly when applied to organic materials.

5.1 Summary

In Chapter 1, some of the basic concepts of thermal transport and pump-probe experiments that were used Chapters 3 and 4 were introduced. Vibrational modes and their behavior as thermal energy carriers were described. The thermal boundary conductance was defined and its importance in nanoscale systems was emphasized. The relationship between the thermotransmittance signal and the thermo-optic coefficient was derived. Several direct applications were then discussed which were used to motivate this work.

Chapter 2 provided details of time-domain thermotransmittance (TDTT), an optical pump-probe thermometry technique well-suited for thermal measurements of nanoscale material systems. The TDTT experiment was adapted from an existing time-domain thermoreflectance (TDTR) setup and was used for all of the thermal measurements in this thesis. The main components of the setup were discussed. A derivation of the thermal transport model for a nanofluid was presented. Sources of noise were described.

In Chapter 3, diffusive thermal transport in fullerene solutions was demonstrated. TDTT measurements reveal thermal boundary conductances that span ~13 to 63 MW m^{-2} K^{-1} and can be tuned by functionalizing C_{60} molecules with different groups. The thermal boundary conductance between fullerene molecules and the surrounding liquid was discussed in terms of the bridging between vibrational modes in the molecule and the liquid. The addition of ester functional groups provides low frequency vibrational modes (near zero) that strongly overlap with the vibrational modes supported by the liquid.

Chapter 4 is concerned with the connection between TDTT measurements of protein films, the thermo-optic coefficient, and the crystallinity index. By relating the thermotransmittance signal to the thermo-optic coefficient, it is observed that TDTT measurements can be used to compare the crystallinity of different semi-crystalline protein aggregates.

5.2 Impact

The major impact of this work is in elucidating the power and adaptability of optical pump-probe thermometry techniques. A modular transmission detection setup provides an easy way to switch between TDTR and TDTT measurements. Further, between both experiments, almost any material system can be studied with the right materials processing expertise. The focus of this thesis was on organic materials, namely fullerene derivative solutions and protein aggregates. TDTT provided the means to make novel observations of the thermophysical properties that define these material systems. In the work from Chapter 3, diffusive thermal transport between a molecule and a liquid was demonstrated for the first time. Moreover, the functionalization of C_{60} molecules can increase the thermal boundary conductance four-fold. While there are certainly other considerations for photothermal agents, these thermal properties are ideal for such an application. As shown in the work from Chapter 4, TDTT can be used to detect crystallinity in protein aggregates. Additionally, this was demonstrated *in vivo* for the first time. This work paves the way for optical pump-probe thermometry as a way to screen abnormal cells in a medical application. Comparatively, these TDTT measurements could potentially be performed much quick than traditional alternatives to identify abnormal tissues.

5.3 Future Projects

The work from my thesis has provoked thought into a few interesting opportunities for future projects that are worth mentioning. Most of these are ideas that were thought of during the fullerene solutions study. However, fullerenes may or may not be the best system to observe these phenomena.

Crowding Effects in Nanofluids

While special care was taken to ensure that the solutions studied in Chapter 3 were in the dilute limit, it would be interesting to investigate what happens when a semidilute concentration is reached and nanoparticles begin to interact with each other. Particularly, how does the effective thermal boundary conductance change? Is it possible to gain insight into the thermal transport mechanisms of the corresponding solid phase (i.e. the limit of a fully dense solid consisting of the nanoparticle material)? If such an investigation is possible, molecular dynamics would be a great compliment to such experimental work.

Phase Transitions in Nanofluids

Along a similar vein as the project described above, the crossover between the thermal transport mechanisms of nanofluids and solids could be investigated by freezing (or melting) a material. One downfall of increasing the concentration of a solution is that it eventually becomes optically opaque. An alternative could be to reduce the temperature past the melting point to transition from a liquid to a solid. Assuming the solvent remains transparent, there would be completely different vibrational characteristics of the solvent and, conceivably, different effective thermal boundary conductances between the nanoparticles and the frozen solvent.

Carrier Nonequilibrium in Nanofluids

Although I only used the two-color TDTT setup and focused on the thermal diffusion time regime, TDTT has historically been used to study carrier nonequilibrium (e.g. electron-phonon coupling). The ExSiTE Lab currently has the capability of performing pump-probe measurements at many different wavelengths. Such experiments might be used to probe hot electron dynamics or electron-vibrational mode coupling in nanofluids. Much like the work in Chapter 3, the presence of functional groups on C_{60}

molecules would be expected to alter the coupling of electrons with vibrational modes in the molecule.

Bibliography

[1] P.E. Hopkins and J.C. Duda, Introduction to Nanoscale Thermal Conduction. In *Heat Transfer: Mathematical Modeling, Numberical Methods and Information Technology*, 2011; p 305.

[2] G. Chen, *Nanoscale Energy Transport and Conversion: A Parallel Treatment of Electrons, Molecules, Phonons, and Photons*. Oxford University Press: New York, 2005.

[3] J.M. Ziman, *Electrons and Phonons*. 1 ed.; Clarendon Press: Oxford, 1960.

[4] G.P. Srivastava, *The Physics of Phonons*. Taylor and Francis: New York, 1990.

[5] P.E. Hopkins. Thermal Transport across Solid Interfaces with Nanoscale Imperfections: Effects of Roughness, Disorder, Dislocations, and Bonding on Thermal Boundary Conductance. *ISRN Mechanical Engineering* **2013**, 19 (2013).

[6] P.L. Kapitza. The Study of Heat Transfer in Helium II. *Zhurnal eksperimentalnoi i teoreticheskoi fiziki* **11**, 1-31 (1941).

[7] E. Hecht, *Optics*. ADDISON WESLEY Publishing Company Incorporated: 2016.

[8] P.B. Allen, J.L. Feldman, J. Fabian, and F. Wooten. Diffusons, Locons and Propagons: Character of Atomie Yibrations in Amorphous Si. *Philosophical Magazine Part B* **79**, 1715-1731 (1999).

[9] C.A. Paddock and G.L. Eesley. Transient Thermoreflectance from Thin Metal Films. *Journal of Applied Physics* **60**, 285-290 (1986).

[10] C.A. Paddock and G.L. Eesley. Transient Thermoreflectance from Metal Films. *Optics Letters* **11**, 273-275 (1986).

[11] D.G. Cahill, P.V. Braun, G. Chen, D.R. Clarke, S. Fan, K.E. Goodson, P. Keblinski, W.P. King, G.D. Mahan, A. Majumdar, H.J. Maris, S.R. Phillpot, E. Pop, and L. Shi. Nanoscale Thermal Transport. II. 2003-2012. *Applied Physics Reviews* **1**, 011305 (2014).

[12] D.G. Cahill, W.K. Ford, K.E. Goodson, G.D. Mahan, A. Majumdar, H.J. Maris, R. Merlin, and S.R. Phillpot. Nanoscale Thermal Transport. *Journal of Applied Physics* **93**, 793-818 (2003).

[13] D.G. Cahill, K.E. Goodson, and A. Majumdar. Thermometry and Thermal Transport in Micro/Nanoscale Solid-State Devices and Structures. *Journal of Heat Transfer* **124**, 223 (2002).

[14] Y.K. Koh, S.L. Singer, W. Kim, J.M.O. Zide, H. Lu, D.G. Cahill, A. Majumdar, and A.C. Gossard. Comparison of the 3ω Method and Time-Domain Thermoreflectance for

Measurements of the Cross-Plane Thermal Conductivity of Epitaxial Semiconductors. *Journal of Applied Physics* **105**, 054303 (2009).

[15] D.G. Cahill. Analysis of Heat Flow in Layered Structures for Time-Domain Thermoreflectance. *Review of Scientific Instruments* **75**, 5119-5122 (2004).

[16] P.E. Hopkins, J.R. Serrano, L.M. Phinney, S.P. Kearney, T.W. Grasser, and C.T. Harris. Criteria for Cross-Plane Dominated Thermal Transport in Multilayer Thin Film Systems During Modulated Laser Heating. *Journal of Heat Transfer* **132**, 081302-081302 (2010).

[17] A.J. Schmidt, X. Chen, and G. Chen. Pulse Accumulation, Radial Heat Conduction, and Anisotropic Thermal Conductivity in Pump-Probe Transient Thermoreflectance. *Review of Scientific Instruments* **79**, 114902 (2008).

[18] C.J. Szwejkowski, N.C. Creange, K. Sun, A. Giri, B.F. Donovan, C. Constantin, and P.E. Hopkins. Size Effects in the Thermal Conductivity of Gallium Oxide (β-Ga_2O_3) Films Grown Via Open-Atmosphere Annealing of Gallium Nitride. *Journal of Applied Physics* **117**, 084308 (2015).

[19] B.F. Donovan, C.J. Szwejkowski, J.C. Duda, R. Cheaito, J.T. Gaskins, C.-Y. Peter Yang, C. Constantin, R.E. Jones, and P.E. Hopkins. Thermal Boundary Conductance across Metal-Gallium Nitride Interfaces from 80 to 450 K. *Applied Physics Letters* **105**, 203502 (2014).

[20] B.M. Foley, C.S. Gorham, J.C. Duda, R. Cheaito, C.J. Szwejkowski, C. Constantin, B. Kaehr, and P.E. Hopkins. Protein Thermal Conductivity Measured in the Solid State Reveals Anharmonic Interactions of Vibrations in a Fractal Structure. *The Journal of Physical Chemistry Letters* **5**, 1077-1082 (2014).

[21] A. Giri, J.-P. Niemelä, C.J. Szwejkowski, M. Karppinen, and P.E. Hopkins. Reduction in Thermal Conductivity and Tunable Heat Capacity of Inorganic/Organic Hybrid Superlattices. *Physical Review B* **93**, 024201 (2016).

[22] A. Giri, J.T. Gaskins, B.F. Donovan, C. Szwejkowski, R.J. Warzoha, M.A. Rodriguez, J. Ihlefeld, and P.E. Hopkins. Mechanisms of Nonequilibrium Electron-Phonon Coupling and Thermal Conductance at Interfaces. *Journal of Applied Physics* **117**, 105105 (2015).

[23] G.-M. Choi, B.-C. Min, K.-J. Lee, and D.G. Cahill. Spin Current Generated by Thermally Driven Ultrafast Demagnetization. *Nat Commun* **5**, (2014).

[24] G.T. Hohensee, W.-P. Hsieh, M.D. Losego, and D.G. Cahill. Interpreting Picosecond Acoustics in the Case of Low Interface Stiffness. *Review of Scientific Instruments* **83**, 114902 (2012).

[25] K.E. O’Hara, X. Hu, and D.G. Cahill. Characterization of Nanostructured Metal Films by Picosecond Acoustics and Interferometry. *Journal of Applied Physics* **90**, 4852-4858 (2001).

[26] S.T. Huxtable, D.G. Cahill, S. Shenogin, and P. Keblinski. Relaxation of Vibrational Energy in Fullerene Suspensions. *Chemical Physics Letters* **407**, 129 (2005).

[27] Z. Ge, D.G. Cahill, and P.V. Braun. Aupd Metal Nanoparticles as Probes of Nanoscale Thermal Transport in Aqueous Solution. *Journal of Physical Chemistry B* **108**, 18870-18875 (2004).

[28] Z. Ge, Y. Kang, T.A. Taton, P.V. Braun, and D.G. Cahill. Thermal Transport in Au-Core Polymer-Shell Nanoparticles. *Nano Letters* **5**, 531-535 (2005).

[29] O.M. Wilson, X. Hu, D.G. Cahill, and P.V. Braun. Colloidal Metal Particles as Probes of Nanoscale Thermal Transport in Fluids. *Physical Review B* **66**, 224301 (2002).

[30] X. Huang, I.H. El-Sayed, W. Qian, and M.A. El-Sayed. Cancer Cell Imaging and Photothermal Therapy in the near-Infrared Region by Using Gold Nanorods. *Journal of the American Chemical Society* **128**, 2115-2120 (2006).

[31] X. Huang, P.K. Jain, I.H. El-Sayed, and M.A. El-Sayed. Plasmonic Photothermal Therapy (PPTT) Using Gold Nanoparticles. *Lasers in Medical Science* **23**, 217 (2007).

[32] P.K. Jain, X. Huang, I.H. El-Sayed, and M.A. El-Sayed. Noble Metals on the Nanoscale: Optical and Photothermal Properties and Some Applications in Imaging, Sensing, Biology, and Medicine. *Accounts of Chemical Research* **41**, 1578-1586 (2008).

[33] D. Jaque, L. Martinez Maestro, B. del Rosal, P. Haro-Gonzalez, A. Benayas, J.L. Plaza, E. Martin Rodriguez, and J. Garcia Sole. Nanoparticles for Photothermal Therapies. *Nanoscale* **6**, 9494-9530 (2014).

[34] C. Loo, A. Lowery, N. Halas, J. West, and R. Drezek. Immunotargeted Nanoshells for Integrated Cancer Imaging and Therapy. *Nano Letters* **5**, 709-711 (2005).

[35] S.T. Huxtable, D.G. Cahill, S. Shenogin, L. Xue, R. Ozisik, P. Barone, M. Usrey, M.S. Strano, G. Siddons, M. Shim, and P. Keblinski. Interfacial Heat Flow in Carbon Nanotube Suspensions. *Nature Materials* **2**, 731 (2003).

[36] C.J. Szwejkowski, A. Giri, R. Warzoha, B.F. Donovan, B. Kaehr, and P.E. Hopkins. Molecular Tuning of the Vibrational Thermal Transport Mechanisms in Fullerene Derivative Solutions. *ACS Nano* **11**, 1389-1396 (2017).

[37] T.F. Krauss. Slow Light in Photonic Crystal Waveguides. *Journal of Physics D: Applied Physics* **40**, 2666 (2007).

[38] H. Ma, A.K.Y. Jen, and L.R. Dalton. Polymer-Based Optical Waveguides: Materials, Processing, and Devices. *Advanced Materials* **14**, 1339-1365 (2002).

[39] Y.A. Vlasov, M. O'Boyle, H.F. Hamann, and S.J. McNab. Active Control of Slow Light on a Chip with Photonic Crystal Waveguides. *Nature* **438**, 65 (2005).

[40] G.T. Reed, G. Mashanovich, F.Y. Gardes, and D.J. Thomson. Silicon Optical Modulators. *Nature Photonics* **4**, 518 (2010).

[41] T. Nikolajsen, K. Leosson, and S.I. Bozhevolnyi. Surface Plasmon Polariton Based Modulators and Switches Operating at Telecom Wavelengths. *Applied Physics Letters* **85**, 5833-5835 (2004).

[42] H. Jung, C.J. Szwejkowski, A. Pena-Francesch, J.A. Tomko, B. Allen, S.K. Ozdemir, P. Hopkins, and M.C. Demirel. Ultrafast Laser-Probing Spectroscopy for Studying Molecular Structure of Protein Aggregates. *Analyst* **142**, 1434-1441 (2017).

[43] D. Randall, W.W. Burggren, K. French, and R. Eckert, *Eckert Animal Physiology*. W. H. Freeman: 2002.

[44] R.M. Costescu, M.A. Wall, and D.G. Cahill. Thermal Conductance of Epitaxial Interfaces. *Physical Review B* **67**, 054302 (2003).

[45] R.M. Costescu, D.G. Cahill, F.H. Fabreguette, Z.A. Sechrist, and S.M. George. Ultra-Low Thermal Conductivity in W/Al_2O_3 Nanolaminates. *Science* **303**, 989-990 (2004).

[46] S.T. Huxtable, D.G. Cahill, and L.M. Phinney. Thermal Contact Conductance of Adhered Microcantilevers. *Journal of Applied Physics* **95**, 2102-2108 (2004).

[47] S. Huxtable, D.G. Cahill, V. Fauconnier, J.O. White, and J.-C. Zhao. Thermal Conductivity Imaging at Micrometre-Scale Resolution for Combinatorial Studies of Materials. *Nature Materials* **3**, 298 (2004).

[48] A. Schmidt, M. Chiesa, X. Chen, and G. Chen. An Optical Pump-Probe Technique for Measuring the Thermal Conductivity of Liquids. *Review of Scientific Instruments* **79**, 064902 (2008).

[49] A.J. Schmidt, J.D. Alper, M. Chiesa, G. Chen, S.K. Das, and K. Hamad-Schifferli. Probing the Gold Nanorod−Ligand−Solvent Interface by Plasmonic Absorption and Thermal Decay. *The Journal of Physical Chemistry C* **112**, 13320-13323 (2008).

[50] User's Manual: Model Sr844 Rf Lock-in Amplifier. revision 2.6 edition ed.; Stanford Research Systems: Sunnyvale, California, 2003.

[51] S. Park, M. Pelton, M. Liu, P. Guyot-Sionnest, and N.F. Scherer. Ultrafast Resonant Dynamics of Surface Plasmons in Gold Nanorods. *The Journal of Physical Chemistry C* **111**, 116-123 (2007).

[52] J.H. Hodak, A. Henglein, and G.V. Hartland. Electron-Phonon Coupling Dynamics in Very Small (between 2 and 8 nm) Diameter Au Nanoparticles. *Journal of Chemical Physics* **112**, 5942-5947 (2000).

[53] J.L. Braun and P.E. Hopkins. Upper Limit to the Thermal Penetration Depth During Modulated Heating of Multilayer Thin Films with Pulsed and Continuous Wave Lasers: A Numerical Study. *Journal of Applied Physics* **121**, 175107 (2017).

[54] H.S. Carslaw and J.C. Jaeger. Conduction of Heat in Solids. *Oxford: Clarendon Press, 1959, 2nd ed.* (1959).

[55] R. Haberman, *Applied Partial Differential Equations with Fourier Series and Boundary Value Problems*. Pearson Higher Ed: 2012.

[56] E. Gramsch. Noise Characteristics of Avalanche Photodiode Arrays of the Bevel-Edge Type. *IEEE Transactions on Electron Devices* **45**, 1587-1594 (1998).

[57] P. Bak, C. Tang, and K. Wiesenfeld. Self-Organized Criticality: An Explanation of the $1/f$ Noise. *Physical Review Letters* **59**, 381-384 (1987).

[58] R.B. Visvesvara and R. Rao, *Signals and Systems*. Prentice-Hall: 1983.

[59] P. Horowitz and W. Hill, *The Art of Electronics*. Cambridge University Press: 2015.

[60] H.W. Kroto, J.R. Heath, S.C. O'Brien, R.F. Curl, and R.E. Smalley. C60: Buckminsterfullerene. *Nature* **318**, 162-163 (1985).

[61] A. Barbot, C. Di Bin, B. Lucas, B. Ratier, and M. Aldissi. N-Type Doping and Thermoelectric Properties of Co-Sublimed Cesium-Carbonate-Doped Fullerene. *Journal of Materials Science* **48**, 2785-2789 (2013).

[62] T. Itoh, K. Ishikawa, and A. Okada. Effect of Fullerene Addition on Thermoelectric Properties of N-Type Skutterudite Compound. *Journal of Materials Research* **22**, 249-253 (2007).

[63] D.T. Morelli. Thermoelectric Power of Superconducting Fullerenes. *Physical Review B* **49**, 655-657 (1994).

[64] E. Park, J. Shim, H. Park, and Y. Park. Thermoelectric Power and Conductivity of the Alkali Metal-Doped Bulk Fullerenes, K X C 60 and Na X C 60. *Synthetic Metals* **44**, 363-368 (1991).

[65] S.K. Yee, J.A. Malen, A. Majumdar, and R.A. Segalman. Thermoelectricity in Fullerene–Metal Heterojunctions. *Nano Letters* **11**, 4089-4094 (2011).

[66] F. Machui, S. Rathgeber, N. Li, T. Ameri, and C.J. Brabec. Influence of a Ternary Donor Material on the Morphology of a P3HT:PCBM Blend for Organic Photovoltaic Devices. *Journal of Materials Chemistry* **22**, 15570-15577 (2012).

[67] M.T. Sajjad, A.J. Ward, C. Kästner, A. Ruseckas, H. Hoppe, and I.D.W. Samuel. Controlling Exciton Diffusion and Fullerene Distribution in Photovoltaic Blends by Side Chain Modification. *Journal of Physical Chemistry Letters* **6**, 3054-3060 (2015).

[68] D.M. Guldi. Fullerene-Porphyrin Architectures; Photosynthetic Antenna and Reaction Center Models. *Chemical Society Reviews* **31**, 22-36 (2002).

[69] P.A. Cox, M.S. Glaz, J.S. Harrison, S.R. Peurifoy, D.C. Coffey, and D.S. Ginger. Imaging Charge Transfer State Excitations in Polymer/Fullerene Solar Cells with Time-Resolved Electrostatic Force Microscopy. *Journal of Physical Chemistry Letters* **6**, 2852-2858 (2015).

[70] G. Dennler, A. Mozer, G. Juška, A. Pivrikas, R. Österbacka, A. Fuchsbauer, and N. Sariciftci. Charge Carrier Mobility and Lifetime Versus Composition of Conjugated Polymer/Fullerene Bulk-Heterojunction Solar Cells. *Organic Electronics* **7**, 229-234 (2006).

[71] M. Lenes, G. Wetzelaer, F.B. Kooistra, S.C. Veenstra, J.C. Hummelen, and P. Blom. Fullerene Bisadducts for Enhanced Open-Circuit Voltages and Efficiencies in Polymer Solar Cells. *Advanced Materials* **20**, 2116 (2008).

[72] N.C. Shukla and S.T. Huxtable, Fullerene Suspensions. In *Handbook of Nanophysics: Clusters and Fullerenes*, K.D. Sattler, Ed. CRC press: 2010; pp 1-10.

[73] C.B. Simon, A. Arzhang, G.A.D. Briggs, A.B. David, G. Daniel, J. John, A.G.J. Mark, F.L. David, W.L. Brendon, N.K. Andrei, S.A. Lyon, J.L.M. John, P. Kyriakos, R.S. Mark, and M.T. Alexei. Towards a Fullerene-Based Quantum Computer. *Journal of Physics: Condensed Matter* **18**, S867 (2006).

[74] E. Nakamura and H. Isobe. Functionalized Fullerenes in Water. The First 10 Years of Their Chemistry, Biology, and Nanoscience. *Accounts of Chemical Research* **36**, 807-815 (2003).

[75] M. Prato and M. Maggini. Fulleropyrrolidines: A Family of Full-Fledged Fullerene Derivatives. *Accounts of Chemical Research* **31**, 519-526 (1998).

[76] S. Bosi, T. Da Ros, G. Spalluto, and M. Prato. Fullerene Derivatives: An Attractive Tool for Biological Applications. *European Journal of Medicinal Chemistry* **38**, 913-923 (2003).

[77] T. Da Ros and M. Prato. Medicinal Chemistry with Fullerenes and Fullerene Derivatives. *Chemical Communications* 663-669 (1999).

[78] S.H. Friedman, D.L. DeCamp, R.P. Sijbesma, G. Srdanov, F. Wudl, and G.L. Kenyon. Inhibition of the HIV-1 Protease by Fullerene Derivatives: Model Building Studies and Experimental Verification. *Journal of the American Chemical Society* **115**, 6506-6509 (1993).

[79] Y. Chai, T. Guo, C. Jin, R.E. Haufler, L.P.F. Chibante, J. Fure, L. Wang, J.M. Alford, and R.E. Smalley. Fullerenes with Metals Inside. *Journal of Physical Chemistry* **95**, 7564-7568 (1991).

[80] H. Shinohara. Endohedral Metallofullerenes. *Reports on Progress in Physics* **63**, 843 (2000).

[81] K. Yamamoto, H. Funasaka, T. Takahashi, and T. Akasaka. Isolation of an ESR-Active Metallofullerene of La@C_{82}. *Journal of Physical Chemistry* **98**, 2008-2011 (1994).

[82] K. Ghaffarzadeh *Graphene, 2D Materials and Carbon Nanotubes: Markets, Technologies and Opportunities 2016-2026*; IDTechEx: 2016.

[83] G. Dennler, M.C. Scharber, and C.J. Brabec. Polymer-Fullerene Bulk-Heterojunction Solar Cells. *Advanced Materials* **21**, 1323-1338 (2009).

[84] M. Campoy-Quiles, T. Ferenczi, T. Agostinelli, P.G. Etchegoin, Y. Kim, T.D. Anthopoulos, P.N. Stavrinou, D.D.C. Bradley, and J. Nelson. Morphology Evolution Via Self-Organization and Lateral and Vertical Diffusion in Polymer:Fullerene Solar Cell Blends. *Nature Materials* **7**, 158-164 (2008).

[85] Y. Shen, K. Li, N. Majumdar, J.C. Campbell, and M.C. Gupta. Bulk and Contact Resistance in P3HT:PCBM Heterojunction Solar Cells. *Solar Energy Materials and Solar Cells* **95**, 2314-2317 (2011).

[86] H.-J. Liu, U.S. Jeng, N.L. Yamada, A.-C. Su, W.-R. Wu, C.-J. Su, S.-J. Lin, K.-H. Wei, and M.-Y. Chiu. Surface and Interface Porosity of Polymer/Fullerene-Derivative Thin Films Revealed by Contrast Variation of Neutron and X-Ray Reflectivity. *Soft Matter* **7**, 9276-9282 (2011).

[87] J.C. Duda, P.E. Hopkins, Y. Shen, and M.C. Gupta. Thermal Transport in Organic Semiconducting Polymers. *Applied Physics Letters* **102**, 251912 (2013).

[88] J.C. Duda, P.E. Hopkins, Y. Shen, and M.C. Gupta. Exceptionally Low Thermal Conductivity of Films of the Fullerene Derivative PCBM. *Physical Review Letters* **110**, 015902 (2013).

[89] J.-H. Pohls, M.B. Johnson, and M.A. White. Origins of Ultralow Thermal Conductivity in Bulk [6,6]-Phenyl-C_{61}-Butyric Acid Methyl Ester (PCBM). *Physical Chemistry Chemical Physics* **18**, 1185-1190 (2016).

[90] J.R. Olson, K.A. Topp, and R.O. Pohl. Specific Heat and Thermal Conductivity of Solid Fullerenes. *Science* **259**, 1145 (1993).

[91] X. Wang, C.D. Liman, N.D. Treat, M.L. Chabinyc, and D.G. Cahill. Ultralow Thermal Conductivity of Fullerene Derivatives. *Physical Review B* **88**, 075310 (2013).

[92] L. Chen, X. Wang, and S. Kumar. Thermal Transport in Fullerene Derivatives Using Molecular Dynamics Simulations. *Scientific Reports* **5**, 12763 (2015).

[93] Y. Gao and B. Xu. Probing Thermal Conductivity of Fullerene C_{60} Hosting a Single Water Molecule. *Journal of Physical Chemistry C* **119**, 20466-20473 (2015).

[94] H. Kim, D. Bedrov, G.D. Smith, S. Shenogin, and P. Keblinski. Role of Attached Polymer Chains on the Vibrational Relaxation of a C_{60} Fullerene in Aqueous Solution. *Physical Review B* **72**, 085454 (2005).

[95] S. Shenogin, P. Keblinski, D. Bedrov, and G.D. Smith. Thermal Relaxation Mechanisms and Role of Chemical Functionalization in Fullerene Solutions. *Journal of Chemical Physics* **124**, (2006).

[96] A. Einstein. Elementary Observations on Thermal Molecular Motion in Solids. *Annalen der Physik* **35**, 679-694 (1911).

[97] J.C. Duda and P.E. Hopkins. Systematically Controlling Kapitza Conductance Via Chemical Etching. *Applied Physics Letters* **100**, 111602 (2012).

[98] P.E. Hopkins, J.C. Duda, C.W. Petz, and J.A. Floro. Controlling Thermal Conductance through Quantum Dot Roughening at Interfaces. *Physical Review B* **84**, 035438 (2011).

[99] P.E. Hopkins, L.M. Phinney, J.R. Serrano, and T.E. Beechem. Effects of Surface Roughness and Oxide Layer on the Thermal Boundary Conductance at Aluminum/Silicon Interfaces. *Physical Review B* **82**, 085307 (2010).

[100] P.E. Hopkins, P.M. Norris, R.J. Stevens, T.E. Beechem, and S. Graham. Influence of Interfacial Mixing on Thermal Boundary Conductance across a Chromium/Silicon Interface. *Journal of Heat Transfer* **130**, 062402-062402 (2008).

[101] B.C. Gundrum, D.G. Cahill, and R.S. Averback. Thermal Conductance of Metal-Metal Interfaces. *Physical Review B* **72**, 245426 (2005).

[102] C.S. Gorham, K. Hattar, R. Cheaito, J.C. Duda, J.T. Gaskins, T.E. Beechem, J.F. Ihlefeld, L.B. Biedermann, E.S. Piekos, D.L. Medlin, and P.E. Hopkins. Ion Irradiation of the Native Oxide/Silicon Surface Increases the Thermal Boundary Conductance across Aluminum/Silicon Interfaces. *Physical Review B* **90**, 024301 (2014).

[103] P.E. Hopkins, J.C. Duda, S.P. Clark, C.P. Hains, T.J. Rotter, L.M. Phinney, and G. Balakrishnan. Effect of Dislocation Density on Thermal Boundary Conductance across Gasb/Gaas Interfaces. *Applied Physics Letters* **98**, 161913 (2011).

[104] Z. Su, L. Huang, F. Liu, J.P. Freedman, L.M. Porter, R.F. Davis, and J.A. Malen. Layer-by-Layer Thermal Conductivities of the Group III Nitride Films in Blue/Green Light Emitting Diodes. *Applied Physics Letters* **100**, 201106 (2012).

[105] A. Giri, J.-P. Niemela, T. Tynell, J.T. Gaskins, B.F. Donovan, M. Karppinen, and P.E. Hopkins. Heat-Transport Mechanisms in Molecular Building Blocks of Inorganic/Organic Hybrid Superlattices. *Physical Review B* (2016).

[106] J.T. Gaskins, A. Bulusu, A.J. Giordano, J.C. Duda, S. Graham, and P.E. Hopkins. Thermal Conductance across Phosphonic Acid Molecules and Interfaces: Ballistic Versus

Diffusive Vibrational Transport in Molecular Monolayers. *Journal of Physical Chemistry C* **119**, 20931-20939 (2015).

[107] W.-P. Hsieh, A.S. Lyons, E. Pop, P. Keblinski, and D.G. Cahill. Pressure Tuning of the Thermal Conductance of Weak Interfaces. *Physical Review B* **84**, 184107 (2011).

[108] P.K. Chow, Y. Cardona Quintero, apos, P. Brien, P. Hubert Mutin, M. Lane, R. Ramprasad, and G. Ramanath. Gold-Titania Interface Toughening and Thermal Conductance Enhancement Using an Organophosphonate Nanolayer. *Applied Physics Letters* **102**, 201605 (2013).

[109] M.D. Losego, M.E. Grady, N.R. Sottos, D.G. Cahill, and P.V. Braun. Effects of Chemical Bonding on Heat Transport across Interfaces. *Nature Materials* **11**, 502-506 (2012).

[110] P.J. O'Brien, S. Shenogin, J. Liu, P.K. Chow, D. Laurencin, P.H. Mutin, M. Yamaguchi, P. Keblinski, and G. Ramanath. Bonding-Induced Thermal Conductance Enhancement at Inorganic Heterointerfaces Using Nanomolecular Monolayers. *Nature Materials* **12**, 118-122 (2013).

[111] P.E. Hopkins, M. Baraket, E.V. Barnat, T.E. Beechem, S.P. Kearney, J.C. Duda, J.T. Robinson, and S.G. Walton. Manipulating Thermal Conductance at Metal–Graphene Contacts Via Chemical Functionalization. *Nano Letters* **12**, 590-595 (2012).

[112] Z. Tian, A. Marconnet, and G. Chen. Enhancing Solid-Liquid Interface Thermal Transport Using Self-Assembled Monolayers. *Applied Physics Letters* **106**, 211602 (2015).

[113] H. Harikrishna, W.A. Ducker, and S.T. Huxtable. The Influence of Interface Bonding on Thermal Transport through Solid–Liquid Interfaces. *Applied Physics Letters* **102**, 251606 (2013).

[114] Z. Ge, D.G. Cahill, and P.V. Braun. Thermal Conductance of Hydrophilic and Hydrophobic Interfaces. *Physical Review Letters* **96**, 186101 (2006).

[115] J. Park and D.G. Cahill. Plasmonic Sensing of Heat Transport at Solid–Liquid Interfaces. *Journal of Physical Chemistry C* **120**, 2814-2821 (2016).

[116] A. Giri and P.E. Hopkins. Spectral Analysis of Thermal Boundary Conductance Across Solid/Classical Liquid Interfaces: A Molecular Dynamics Study. *Applied Physics Letters* **105**, 033106 (2014).

[117] J.V. Goicochea, M. Hu, B. Michel, and D. Poulikakos. Surface Functionalization Mechanisms of Enhancing Heat Transfer at Solid-Liquid Interfaces. *Journal of Heat Transfer* **133**, 082401-082401 (2011).

[118] N. Shenogina, R. Godawat, P. Keblinski, and S. Garde. How Wetting and Adhesion Affect Thermal Conductance of a Range of Hydrophobic to Hydrophilic Aqueous Interfaces. *Physical Review Letters* **102**, 156101 (2009).

[119] N.B. Vargaftik, *Handbook of Thermal Conductivity of Liquids and Gases*. CRC press: 1993.

[120] P.E. Hopkins. Influence of Inter- and Intraband Transitions to Electron Temperature Decay in Noble Metals after Short-Pulsed Laser Heating. *Journal of Heat Transfer* **132**, 122402-122402 (2010).

[121] C.I. Wang and C.C. Hua. Solubility of C_{60} and PCBM in Organic Solvents. *Journal of Physical Chemistry B* **119**, 14496-14504 (2015).

[122] K.N. Semenov, N.A. Charykov, V.A. Keskinov, A.K. Piartman, A.A. Blokhin, and A.A. Kopyrin. Solubility of Light Fullerenes in Organic Solvents. *Journal of Chemical and Engineering Data* **55**, 13-36 (2010).

[123] J.C. Hummelen, B.W. Knight, F. LePeq, F. Wudl, J. Yao, and C.L. Wilkins. Preparation and Characterization of Fulleroid and Methanofullerene Derivatives. *Journal of Organic Chemistry* **60**, 532-538 (1995).

[124] D.R. Klein, Uv-Vis Spectroscopy. In *Organic Chemistry*, 1st ed.; John Wiley & Son's Inc.: United States of America, 2012; pp 800-805.

[125] L.F. Fieser, M. Fieser, and S. Rajagopalan. Absorption Spectroscopy and the Structures of the Diosterols. *Journal of Organic Chemistry* **13**, 800-806 (1948).

[126] R.B. Woodward. Structure and Absorption Spectra. III. Normal Conjugated Dienes. *Journal of the American Chemical Society* **64**, 72-75 (1942).

[127] S. Abe, B. Burger, S.L. Dexheimer, G. Dresselhaus, M.S. Dresselhaus, P.C. Eklund, Z. Guo, Z.H. Kafifa, S. Kazaoui, V. Klimov, R. Kohlman, J. Kürti, H. Kuzmany, P.A. Lane, D. McBranch, N. Minami, J.E. Riggs, H.W. Rollins, R. Saito, N.S. Sariciftci, J. Shinar, L. Smilowitz, F.P. Strohkendl, Y.-P. Sun, Z.V. Vardeny, and R.B. Weisman, *Optical and Electronic Properties of Fullerenes and Fullerene-Based Materials*. Marcel Dekker: New York, NY, 2000.

[128] H. Brands, O.T. Ehrler, M. Kappes, and A.-N. Unterreiner. Relaxation Dynamics of Electronically Excited C_{60}^{-} in *o*-Dichlorobenzene and Tetrahydrofuran Solution. *Zeitschrift fur Physikalische Chemie* **225**, 939 (2011).

[129] H.S. Cho, T.K. Ahn, S.I. Yang, S.M. Jin, D. Kim, S.K. Kim, and H.D. Kim. Singlet Excited State (S1) of Higher Fullerenes C_{76} and C_{84}: Correlation between Lifetime and Homo–Lumo Energy Gap. *Chemical Physics Letters* **375**, 292-298 (2003).

[130] V.M. Farztdinov, Y.E. Lozovik, Y.A. Matveets, A.G. Stepanov, and V.S. Letokhov. Femtosecond Dynamics of Photoinduced Darkening in C_{60} Films. *Journal of Physical Chemistry* **98**, 3290-3294 (1994).

[131] D. Kim, M. Lee, Y.D. Suh, and S.K. Kim. Observation of Fluorescence Emission from Solutions of C_{60} and C_{70} Fullerenes and Measurement of Their Excited-State Lifetimes. *Journal of the American Chemical Society* **114**, 4429-4430 (1992).

[132] V. Klimov, L. Smilowitz, H. Wang, M. Grigorova, J.M. Robinson, A. Koskelo, B.R. Mattes, F. Wudl, and D.W. McBranch. Femtosecond to Nanosecond Dynamics in Fullerenes: Implications for Excitedstate Optical Nonlinearities. *Research on Chemical Intermediates* **23**, 587-600

[133] E. Koudoumas, M. Konstantaki, A. Mavromanolakis, X. Michaut, S. Couris, and S. Leach. Transient and Instantaneous Third-Order Nonlinear Optical Response of C_{60} and the Higher Fullerenes C_{70}, C_{76} and C_{84}. *Journal of Physics B: Atomic, Molecular and Optical Physics* **34**, 4983 (2001).

[134] M. Lee, O.-K. Song, J.-C. Seo, D. Kim, Y.D. Suh, S.M. Jin, and S.K. Kim. Low-Lying Electronically Excited States of C_{60} and C_{70} and Measurement of Their Picosecond Transient Absorption in Solution. *Chemical Physics Letters* **196**, 325-329 (1992).

[135] T. Matsuo, H. Suga, W.I.F. David, R.M. Ibberson, P. Bernier, A. Zahab, C. Fabre, A. Rassat, and A. Dworkin. The Heat Capacity of Solid C_{60}. *Solid State Communications* **83**, 711 (1992).

[136] *Specific Heat - Nonmetallic Solids*. IFI/Plenum: New York, 1970; Vol. 5, p 202.

[137] S. Plimpton. Fast Parallel Algorithms for Short-Range Molecular Dynamics. *Journal of Computational Physics* **117**, 1-19 (1995).

[138] M.P. Allen and D.J. Tildesley, *Computer Simulation of Liquids*. Oxford university press: 1989.

[139] J.C. Duda, T.S. English, E.S. Piekos, W.A. Soffa, L.V. Zhigilei, and P.E. Hopkins. Implications of Cross-Species Interactions on the Temperature Dependence of Kapitza Conductance. *Physical Review B* **84**, 193301 (2011).

[140] S.J. Stuart, A.B. Tutein, and J.A. Harrison. A Reactive Potential for Hydrocarbons with Intermolecular Interactions. *Journal of Chemical Physics* **112**, 6472-6486 (2000).

[141] W.-L. Ong, E.S. O/'Brien, P.S.M. Dougherty, D.W. Paley, C. Fred Higgs Iii, A.J.H. McGaughey, J.A. Malen, and X. Roy. Orientational Order Controls Crystalline and Amorphous Thermal Transport in Superatomic Crystals. *Nature Materials* **16**, (2016).

[142] K. Sääskilahti, J. Oksanen, J. Tulkki, and S. Volz. Spectral Mapping of Heat Transfer Mechanisms at Liquid-Solid Interfaces. *Physical Review E* **93**, 052141 (2016).

[143] J.C. Duda, P.E. Hopkins, J.L. Smoyer, M.L. Bauer, T.S. English, C.B. Saltonstall, and P.M. Norris. On the Assumption of Detailed Balance in Prediction of Diffusive Transmission Probability During Interfacial Transport. *Nanoscale and Microscale Thermophysical Engineering* **14**, 21-33 (2010).

[144] E.T. Swartz and R.O. Pohl. Thermal Boundary Resistance. *Reviews of Modern Physics* **61**, 605-668 (1989).

[145] G.M. Cooper, *The Cell: A Molecular Approach*. ASM Press: 1997.

[146] M.C. Demirel, M. Cetinkaya, A. Pena-Francesch, and H. Jung. Recent Advances in Nanoscale Bioinspired Materials. *Macromolecular Bioscience* **15**, 300-311 (2015).

[147] H. Jung, A. Pena-Francesch, A. Saadat, A. Sebastian, D.H. Kim, R.F. Hamilton, I. Albert, B.D. Allen, and M.C. Demirel. Molecular Tandem Repeat Strategy for Elucidating Mechanical Properties of High-Strength Proteins. *Proceedings of the National Academy of Sciences* **113**, 6478-6483 (2016).

[148] A. Pena-Francesch, B. Akgun, A. Miserez, W. Zhu, H. Gao, and M.C. Demirel. Pressure Sensitive Adhesion of an Elastomeric Protein Complex Extracted from Squid Ring Teeth. *Advanced Functional Materials* **24**, 6227-6233 (2014).

[149] A. Pena-Francesch, S. Florez, H. Jung, A. Sebastian, I. Albert, W. Curtis, and M.C. Demirel. Materials Fabrication from Native and Recombinant Thermoplastic Squid Proteins. *Advanced Functional Materials* **24**, 7401-7409 (2014).

[150] V. Sariola, A. Pena-Francesch, H. Jung, M. Çetinkaya, C. Pacheco, M. Sitti, and M.C. Demirel. Segmented Molecular Design of Self-Healing Proteinaceous Materials. *Scientific Reports* **5**, 13482 (2015).

[151] H. Yılmaz, A. Pena-Francesch, R. Shreiner, H. Jung, Z. Belay, M.C. Demirel, Ş.K. Özdemir, and L. Yang. Structural Protein-Based Whispering Gallery Mode Resonators. *ACS Photonics* **4**, 2179-2186 (2017).

[152] S.B. Dev. Unsolved Problems in Biology—the State of Current Thinking. *Progress in Biophysics and Molecular Biology* **117**, 232-239 (2015).

[153] M.A. Martí-Renom, A.C. Stuart, A. Fiser, R. Sánchez, F.M. and, and A. Šali. Comparative Protein Structure Modeling of Genes and Genomes. *Annual Review of Biophysics and Biomolecular Structure* **29**, 291-325 (2000).

[154] T. Schwede, J.r. Kopp, N. Guex, and M.C. Peitsch. Swiss-Model: An Automated Protein Homology-Modeling Server. *Nucleic Acids Research* **31**, 3381-3385 (2003).

[155] T.L. Blundell and L.N. Johnson, *Protein Crystallography*. Academic Press: 1976.

[156] C.V. Robinson, A. Sali, and W. Baumeister. The Molecular Sociology of the Cell. *Nature* **450**, 973 (2007).

[157] R. Pepperkok and J. Ellenberg. High-Throughput Fluorescence Microscopy for Systems Biology. *Nature Reviews Molecular Cell Biology* **7**, 690 (2006).

[158] G.H. Altman, F. Diaz, C. Jakuba, T. Calabro, R.L. Horan, J. Chen, H. Lu, J. Richmond, and D.L. Kaplan. Silk-Based Biomaterials. *Biomaterials* **24**, 401-416 (2003).

[159] M. Nixon and P. Dilly In *Sucker Surfaces and Prey Capture*, Symposia of the Zoological Society of London, 1977; pp 447-511.

[160] C.Y. Ho and R.E. Taylor, *Thermal Expansion of Solids*. ASM international: 1998; Vol. 4.

[161] J.M. Gosline, M.W. Denny, and M.E. DeMont. Spider Silk as Rubber. *Nature* **309**, 551 (1984).

[162] Z. Zhang, P. Zhao, P. Lin, and F. Sun. Thermo-Optic Coefficients of Polymers for Optical Waveguide Applications. *Polymer* **47**, 4893-4896 (2006).

[163] P.E. Hopkins. Influence of Electron-Boundary Scattering on Thermoreflectance Calculations after Intra- and Interband Transitions Induced by Short-Pulsed Laser Absorption. *Physical Review B* **81**, 035413 (2010).

[164] D.R. Lide, *Crc Handbook for Chemistry and Physics*. 89th ed.; Internet Version, CRC Press/Taylor and Francis: Boca Raton, FL, 2008.

[165] M. Rubinstein and R.H. Colby, *Polymer Physics*. OUP Oxford: 2003.

[166] A.P. Caffrey, P.E. Hopkins, J.M. Klopf, and P.M. Norris. Thin Film Non-Noble Transition Metal Thermophysical Properties. *Microscale Thermophysical Engineering* **9**, 365-377 (2005).

[167] J. Edelman. The Low-Temperature Heat Capacity of Solid Proteins. *Biopolymers* **32**, 209-218 (1992).

[168] T. Kulagina, T. Bykova, and B. Lebedev. [Thermodynamic Functions of Lysozyme, Myoglobin, Beta-Lactoglobulin, Albumin, and Poly-L-Tryptophane in the Temperature Range 0-330 K]. *Biofizika* **46**, 210-215 (2000).

[169] J. Nielsen, M. Fussenegger, J. Keasling, S.Y. Lee, J.C. Liao, K. Prather, and B. Palsson. Engineering Synergy in Biotechnology. *Nature Chemical Biology* **10**, 319 (2014).